Spring 2021

DNA-Origami-Based Fluorescence Brightness Standards for Convenient and Fast Protein Counting in Live Cells

Nathan David Williams
Yale University Graduate School of Arts and Sciences, nate.w@mac.com

Abstract

DNA-Origami-Based Fluorescence Brightness Standards for Convenient and Fast Protein Counting in Live Cells

Nathan David Williams
2021

Fluorescence microscopy has been one of the most discovery-rich methods in biology. In the digital age, the discipline is becoming increasingly quantitative. Virtually all biological laboratories have access to fluorescence microscopes, but abilities to quantify biomolecule copy numbers are limited by the complexity and sophistication associated with current quantification methods. Here, we present DNA-origami-based fluorescence brightness standards for counting 5–300 copies of proteins in bacterial and mammalian cells, tagged with fluorescent proteins or membrane-permeable organic dyes. Compared to conventional quantification techniques, our brightness standards are robust, straightforward to use, and compatible with nearly all fluorescence imaging applications, thereby providing a practical and versatile tool to quantify biomolecules *via* fluorescence microscopy.

DNA-Origami-Based Fluorescence Brightness Standards for Convenient and Fast Protein Counting in Live Cells

A Dissertation
Presented to the Faculty of the Graduate School of
Yale University
in Candidacy for the Degree of
Doctor of Philosophy

by
Nathan David Williams

Dissertation Director:
Chenxiang Lin

June 2021

DESCRIPTION OF PUBLISHED AND UNPUBLISHED RESULTS

The preceding abstract, as well as all results discussed in Chapters 2 through 4, including text, figures, and materials & methods, were published in the following publication:

Williams, N. D., Landajuela, A., Kasula, R. K., Zhou, W., Powell, J. T., Xi, Z., Isaacs, F. J., Berro, J., Toomre, D., Karatekin, E., & Lin, C. (2020). DNA-Origami-Based Fluorescence Brightness Standards for Convenient and Fast Protein Counting in Live Cells. *Nano Letters*. https://doi.org/10.1021/acs.nanolett.0c03925

Attributions

All cloning, culturing, and widefield imaging of B. subtilis cells and mEGFP standards for live cell calibration experiments were performed by Ane Landajuela (Figure 2c & d, 7, S9, S10, Table S3).
Culturing, labeling, and confocal imaging of HeLa cells and SiR standards for live cell calibration experiments were performed by Ravi Kasula (Figure 2c, 9, S12-S18, Table S3).
6hb structure design, expression and purification of mEGFP(pAzF), as well as mEGFP-DNA conjugation and purification, was performed with assistance from Wenjiao Zhou (Figure 2b, S6, S7).
SiR-DNA Conjugate was SDS-PAGE purified by John Powell (Figure S11).
CLC-HaloTag CRISPR cells were generated by Zhiqun Xi (Figure 2c, 9, S12-S18).

Acknowledgements

I would like to extend special thanks to my advisor and family for their unwavering support during my time at Yale. Additionally, I would like to thank my collaborators and lab mates for their assistance and feedback throughout this project.

Table of Contents

Chapter 1: Introduction

1.1 Quantitative Fluorescence Microscopy

History

Since the 17th century, microscopy has been essential to increasing knowledge by shedding light on ever smaller scales. With the advent of fluorescence microscopy over a century ago (Renz, 2013), the power of the microscope increased immensely. Two advancements of similar magnitude were the cloning of the green fluorescent protein (GFP) in 1992 (Prasher et al., 1992), and the wide availability of computer technology to process fluorescence micrographs (Patterson et al., 1997), which enabled the quantification of genomically-tagged biomolecules in cells. Because many biological processes depend on the accumulation and interaction of a discreet number of proteins or protein complexes in a specific location in the cell, the ability to count the players in a given subcellular region proved to be essential to understanding complex processes (Gruβmayer et al., 2019). These technologies led insights in many fields, including more complete models of the octameric nuclear pore complex (V. Coffman et al., 2014; Hoelz et al., 2011). The methods of applying quantitative fluorescence microscopy are diverse, and frequently adapted for unique applications. These include fluorescence correlation spectroscopy (FCS), stepwise photobleaching, quantitative super-resolution, and standardized ratiometric comparison (V. Coffman et al., 2014).

FCS

FCS measures fluorescence intensity of molecules as they diffuse through a very small observation volume (~0.5 fL for confocal-FCS) (Bulseco & Wolf, 2013; B D Slaughter & Li, 2010; Brian D Slaughter et al., 2008; Verdaasdonk et al., 2014). By feeding this data into an autocorrelation function, the self-similarity of the system as a function of time may be calculated to generate a curve whose amplitude describes the variance of fluorescence through time. Finally, this curve is fit to a diffusion model that most accurately describes the system to shed light on local diffusion coefficients, local concentrations, and more (S. A. Kim et al., 2007; Verdaasdonk et al., 2014). Its high sensitivity and spatiotemporal resolution makes FCS a powerful and popular tool for uncovering complex molecular dynamics in real time, but it is not without its limitations (S. A. Kim et al., 2007; Ries & Schwille, 2012; Schwille, 2001; Tian et al., 2011; Verdaasdonk et al., 2014; Vukojević et al., 2005; Zipfel & Webb, 2001). First, the complexity and specificity of the method necessitates an equally complex and specialized microscopy setup (Bacia & Schwille, 2003; Bulseco & Wolf, 2013; Haustein & Schwille, 2007; Verdaasdonk et al., 2014). Second, its reliance on diffusing molecules limits FCS to measuring mobile samples (Verdaasdonk et al., 2014). Third, due to its high sensitivity, intracellular FCS is especially prone to collecting artifacts (S. A. Kim et al., 2007). For instance, because the time required for acquisition is dependent on the concentration and rate of diffusion, particles too far from the ideal concentration (~1 nM) and diffusion rate (10^{-6}–10^{-9} cm^2/s) will require longer scans, which can bleach the sample (Bacia & Schwille, 2003; Ries & Schwille, 2012; Verdaasdonk et al., 2014).

Stepwise Photobleaching

Counting by stepwise photobleaching involves tagging a POI with a fluorophore, then measuring intensity levels as each molecule irreversibly loses fluorescence via bleaching. The number of “stair-steps” in the characteristic trace are then counted to determine the number of molecules. Because the probability of two molecules simultaneously being bleached increases with the number of molecules, this approach is generally limited to 10 or fewer molecules (though up to 30 have been counted in some cases (V. Coffman et al., 2014; Gao et al., 2010; Kurz et al., 2013)), and cannot directly measure global concentrations.

Quantitative Single-molecule localization microscopy

Quantitative Single-molecule localization microscopy (SMLM), aims to expand upon the various techniques’ enhanced resolving power by extracting molecular counts from SMLM datasets. These methods (reviewed in (Khater et al., 2020)) include photoactivated localization microscopy (PALM), stochastic optical reconstruction microscopy (STORM), ground state depletion (GSD), DNA-based point accumulation for imaging in nanoscale topography (DNA-PAINT, see chapter 1.2), and MINFLUX. Each technique shares the same basic principle: fitting thousands of photon collection events to Gaussian functions to approximate the position of each fluorophore. The complex nature of these methods creates more constraints on sample preparation, fluorophore choice, and instrumentation than diffraction-limited microscopy, primarily due to the need to control fluorophore behavior over longer collection times. Further, the statistical analysis of these data is much more intricate and time-consuming than conventional

methods (Jungmann et al., 2016; J. Stein et al., 2019; Wassie et al., 2019; Zanacchi et al., 2017). The power and reach of these methods has yet to be fully realized, primarily due to the difficulty of implementation.

Standardized Ratiometric Comparison

Using an intensity standard overcomes limitations of other methods by not relying on detecting single molecule events. Instead, fluorescence intensities from FP-tagged POIs are compared to measurements of one or more standards with a known number of the same fluorophore to construct a standard curve relating the intensity to fluorophore number. Ratiometric comparison can be used to report local and global concentrations in a number of systems without highly specialized equipment, prompting proponents assert, “Every laboratory with a fluorescence microscope should consider counting molecules.” (V C Coffman & Wu, 2014) The accuracy and precision of ratiometric comparison hinges upon the construction and characterization of fluorescence standards. These may be grouped into 3 types (V C Coffman & Wu, 2014): 1, Single FPs in solution (Lawrimore et al., 2011); 2, a FP-tagged protein in a complex for which the constituents’ stoichiometry is already known (Joglekar et al., 2008); 3, multiple tagged proteins whose concentration is obtained using a complementary approach like quantitative immunoblotting (Akamatsu et al., 2017; V C Coffman & Wu, 2014; Verdaasdonk et al., 2014; Wu & Pollard, 2005). Measuring fluorescence of single FPs in vitro is the most straightforward of the three, and because it is external, it is simpler and may be adapted to many systems with proper controls. Despite these strengths, single FPs can be difficult to image and require complex methods to compensate for the low

signal to noise ratio (Lawrimore et al., 2011; Verdaasdonk et al., 2014), Examples of the second type are the *E. coli* motor protein MotB and yeast histone H3 variant Cse4. MotB's well-established stoichiometry makes it a valuable standard, but its lack of conservation among higher orders limits its scope. Conversely, Cse4 is anticipated to be conserved from yeast to humans (Joglekar et al., 2008; Wieland et al., 2004), but conflicting reports regarding its stoichiometry have hampered its reliability (V C Coffman & Wu, 2014; Verdaasdonk et al., 2014). The third type was originally demonstrated as a tool for counting proteins in fission yeast (*Schizosaccharomyces pombe*) (Akamatsu et al., 2017; Berro & Pollard, 2014; Wu & Pollard, 2005), and has since been adapted to additional systems (Ditlev et al., 2012; Newman et al., 2006). In the original work, the standard curve was constructed using measurements from seven yeast strains, each with a different YFP-tagged reference protein driven from its native promoter. The average intensity/cell and cell volume were ascertained using confocal microscopy and confirmed by flow cytometry, and the average number of molecules/cell was measured by quantitative immunoblotting lysate from a known number of cells (estimated by OD). This approach stands out because of its accuracy (< 2-fold error). Calibrating with several reference proteins is more accurate than a using a single standard (V C Coffman & Wu, 2014; McCormick et al., 2013; Wu & Pollard, 2005) and expression from native promoters means proteins may be measured at their native levels (V C Coffman & Wu, 2014; Valerie C Coffman & Wu, 2012; Verdaasdonk et al., 2014). Furthermore, comparison to mass-spec measurements showed less than a 5-fold difference in most cases, and this discrepancy is likely due to differences in growth media (V. Coffman et

al., 2014; Wu & Pollard, 2005). Despite this strategy's power and flexibility, it is limited primarily by its exigency. First, genomically-tagging multiple POIs is often tedious. Second, because measurements taken on different days have been shown to differ (even when using identical imaging conditions) (Joglekar et al., 2006), calibration should be performed with or immediately before each experiment (V. Coffman et al., 2014). This makes every experiment an all-day affair, beginning with growing all necessary strains, and ending with lysis and immunoblotting. Finally, because signal to noise is dependent on protein number and excitation intensity, this technique is not ideal for counting low copy proteins.

Protein counting by fluorescence microscopy is a powerful tool, but current calibration standards limit its precision and flexibility. To overcome this obstacle, next-generation standards constructed with nanometer precision must be developed.

1.2 Brief History of DNA Nanotechnology

Inspired by the MC Escher woodcut, Depth (Figure 2a) (Escher, 1955), in 1982, Nadrian Seeman proposed that, "It appears to be possible to generate covalently joined three-dimensional networks of nucleic acids which are periodic in connectivity and perhaps in space." (Pinheiro et al., 2011; Seeman, 1982) Little did he know that his assertion would spark an explosion of nanoengineering innovation that continues to this day. Among the most notable early achievements in the field (reviewed in (Fan et al., 2019)) are the 3-arm DNA junction in 1986 (Ma et al., 1986), the enhanced rigidity provided by the double-crossover (DX) in 1993 (Fu & Seeman, 1993), extending the DX motif to a 2-dimensional sheet in 1998 (Winfree et al., 1998), and the 3D octahedron in 2004 (Shih

et al., 2004) (**Figure 1b-e**). The realization of DNA as a nanoscale building material took a macroscale leap in 2006 with the invention of scaffolded DNA origami (Rothemund, 2006), which involves folding a large, circular, single-stranded “scaffold” strand (from M13 phage) into complex shapes using carefully designed short “staple” strands. DNA origami design is greatly facilitated by purpose-built software like caDNAno (Douglas, Marblestone, et al., 2009) & CanDo (D.-N. Kim et al., 2012) and its simple assembly protocol may be completed in hours (Castro et al., 2011; Dietz et al., 2009; Linko & Dietz, 2013; Rothemund, 2006; Wagenbauer et al., 2017), making it a rapid, precise, and inexpensive method to generate nanoscale objects. The possibilities of this new technique were quickly apparent, and the innovation was swift. In the ensuing decade and a half, researchers expanded upon the original work to build in 3-dimensions (Douglas, Dietz, et al., 2009), produce curved objects (Dietz et al., 2009), and eventually, myriad nanoscale devices capable of responding to a wide variety of external stimuli (Ijäs et al., 2018; Singh et al., 2018). The key breakthroughs DNA origami provides are not only the ability to build at the nanometer scale, but the ease with which these objects may be functionalized by the attachment of guest molecules. Perhaps DNA origami’s primary advantage over its primary competing nanoconstruction modality, lithography, is how easily proteins may be incorporated into DNA origami devices. Because of the coded nature of DNA origami, all that is required for guest molecule functionalization is a single stranded DNA ‘handle’ extending from the DNA nanostructure, and the conjugation of a guest molecule to a complementary ‘antihandle’ strand. Subsequently, antihandle-conjugated guest molecules hybridize to their

designed handle sequences following a (usually) short coincubation. This facilitates the creation of all manner of functionalized DNA nanodevices, with many different molecular species attached to predesigned locations along a given DNA nanostructure. This concept has been demonstrated in many different ways, including microscopy standards (Schmied et al., 2014; Zanacchi et al., 2017) and controlled drug delivery devices (Douglas et al., 2012). Because there are already a wide variety of commercially-available, synthetic, DNA-conjugated guest molecules, this work will focus specifically on proteins as guest molecules.

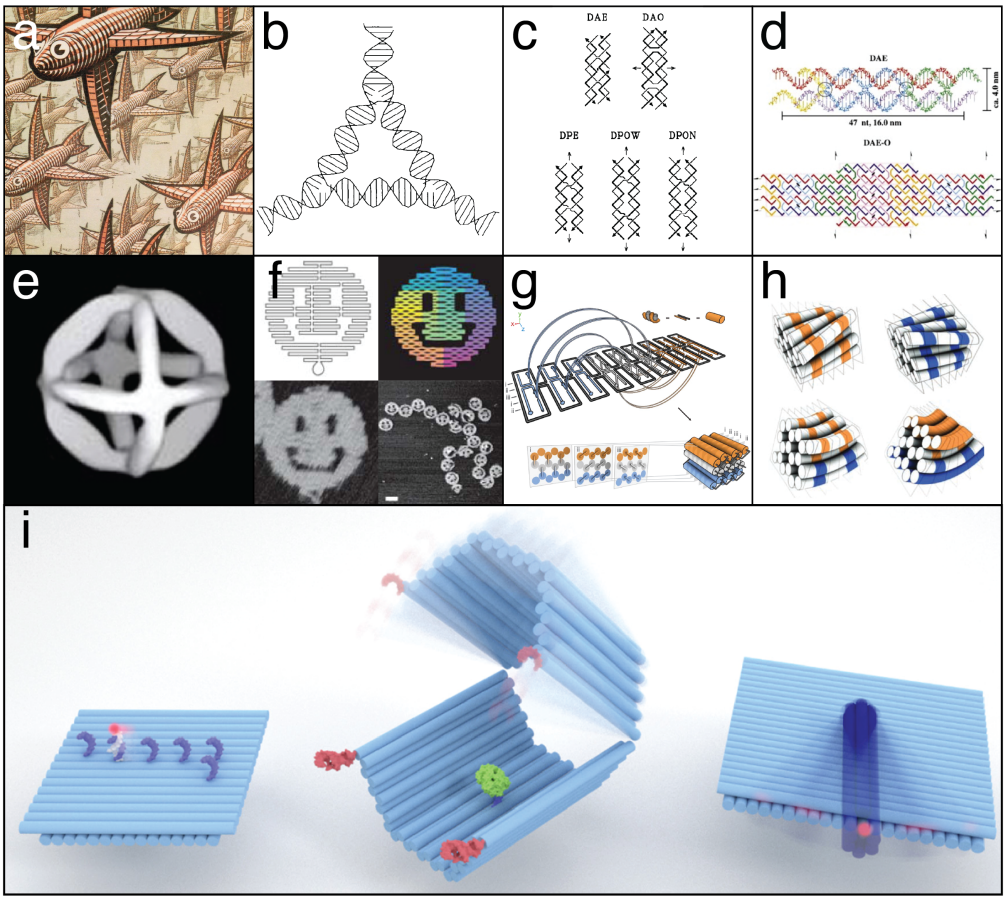

Figure 1: Key Achievements in the History of DNA Nanotechnology
(a) M.C. Escher's woodcut, "Depth" (Escher, 1955). (b) 3-arm junction (Ma et al., 1986). (c) Examples of the five double-crossover (DX) motifs (Fu & Seeman, 1993). (d) Illustration depicting the extension of the DAE DX motif into a 2-dimensional lattice (Winfree et al., 1998). (e) 3D map generated from particle reconstruction of the DNA

octahedron (Shih et al., 2004). (f) Smiley face design from the original DNA origami paper (Rothemund, 2006). (g) 3D DNA Origami (Douglas, Dietz, et al., 2009). (h) Curved DNA Origami (Dietz et al., 2009). (i) 3 examples of environmentally-responsive DNA origami devices. From L to R: a cargo sorting robot (Thubagere et al., 2017), a controlled drug delivery device (Douglas et al., 2012), a robotic arm that rotates in response to a magnetic field (Kopperger et al., 2018). Illustration from (Iljäs et al., 2018). Reproduced with permission.

DNA-Protein Conjugation

A wide variety of conjugation chemistries have been used to conjugate DNA to different guest molecules. Ideally, conjugation should be highly specific, both in where the linkage is placed and stoichiometrically. It should also be amenable to rapid mass production, i.e., highly scalable, and simple enough to perform with minimal additional training. Although the most popular method continues to be maleimide-cysteine conjugation, it suffers from the weakness that many guest molecules either do not contain a cysteine available for conjugation, or contain more than one. This is especially relevant to proteins whose structure and function may be altered by the addition or deletion of surface cysteines, or when the downstream application requires strict control over labeling stoichiometry. Several conjugation methods have been devised to address this issue, including self-labeling tags (SNAP, CLiP, Halo) (Liss et al., 2015), DNA-templated protein conjugation (DTPC) (Rosen et al., 2014; Trads et al., 2017), and conjugation to inserted bio-orthogonal nonstandard amino acids (NSAAs) (Soundrarajan et al., 2012; Wang et al., 2020). Of these more targeted methods, self-labeling tags are currently the most popular, but suffer from the potential drawbacks of the bulk of the tag itself, and the inability to insert the tag in the middle of the protein. This is of particular concern in the design of DNA nanostructures, where a guest molecule's geometry and

conjugation location are key design considerations. DTPC uses a 6xHis-tag-binding, nickel-NTA-conjugated DNA strand to bring a complimentary, reactive DNA strand into close proximity of reactive surface lysines. And so, while conjugation may be targeted in a codon specific manner, it has the same drawback as maleimide-cysteine chemistry, i.e. the addition or removal of reactive amino acids, as well as the need for a 6xHis tag. NSAA conjugation overcomes the constraints of both self-labeling tags and DTPC: it enables conjugation at any amino acid position, and requires only a single amino acid addition or substitution, and in many cases, the substituted NSAA can be identical to the genomic one, save the addition of a reactive group such as an azide. The main caveat to NSAA conjugation is the method of NSAA incorporation. This may be done in vitro, or in-vivo, utilizing one of a number of strategies (reviewed in (Wang et al., 2020)). Perhaps the most elegant approach to NSAA incorporation was developed by the Church and Isaacs labs at Harvard and Yale, respectively. Briefly, the authors systematically mutated all UAG stop codons to UAA in a standard lab strain of *E. coli* and deleted the release factor which terminates translation at UAG. Then, with the introduction of an orthogonal translation system capable of charging amino acids at UAG codons, the codons could be placed wherever a NSAA was desired (Lajoie et al., 2013). These recoded strains may be used to generate proteins with NSAAs at virtually any desired location. This is the system we used to generate DNA-mEGFP conjugates for the creation of DNA origami brightness standards (Williams et al., 2020).

1.3 Context and Significance of Our Work

DNA Nanotechnology and Quantitative Fluorescence Microscopy

The ability to design objects with defined structure and function on the nanometer scale makes it DNA origami an ideal platform for microscopy standards, as shown in recent in vitro studies (reviewed in (Schlichthaerle et al., 2016)). Among the major innovations are organic dye brightness standards (Schmied et al., 2012), nanorulers for FRET-specific and generalized distance calibration (Schmied et al., 2014; I. H. Stein et al., 2011), nanobarcodes (Lin et al., 2012), immunofluorescence calibration standards (Zanacchi et al., 2017), and DNA-PAINT (Jungmann et al., 2010), which has seen multiple enhancements since its introduction (Auer et al., 2018; Chung et al., 2020; Jungmann et al., 2014, 2016; Liu et al., 2019).

Significance of Our Work

The various methods described above are powerful in their own right, but suffer from the same key weakness, which we hope to address with the following work. The common weakness is the high barrier to entry, that is, many labs currently using fluorescence microscopes do not quantify their protein targets because of the time, cost, and difficulty in doing so. As we stated in (Williams et al., 2020), "…there is a pressing need for a fast, universal technique that can be conveniently integrated into a wide array of existing imaging workflows to count biomolecules." Our system provides a fast, simple way to quantify protein targets ranging from 5-300 molecules being imaged by labs across the globe. It requires little to no additional cloning, and can be adapted for virtually any fluorophore, be they fluorescent proteins or organic dyes. Additionally, they may be stored long term until needed, which means a typical lab could go from imaging

a new target for the first time to having accurate counts in mere hours (Williams et al., 2020).

Chapter 2: A GFP Standard

2.1 Design of the DNA-origami based standards

The design of our DNA-origami structures for generating brightness standards is based on the well-documented 6 helix-bundle (6hb) nanotube, which is ~7 nm in diameter and ~407 nm long (Douglas et al., 2007; Lin et al., 2012; Mathieu et al., 2005; Rothemund, 2006) (**Figure 2a** & **S1**–**S4**). Previously, 6hb and other rod-shaped DNA-origami structures have been used to construct fluorescence markers and barcodes for bioimaging, (Jusuk et al., 2015; Lin et al., 2012; Schmied et al., 2012, 2013; Woehrstein et al., 2017; Zanacchi et al., 2017) owing to their robust assembly (up to 90% yield) as well as their thermal (melting temperature ≈ 60°C) (Werner et al., 2012) and mechanical stability (persistence length>1 μm) (Czogalla et al., 2013). In these applications, single-stranded extensions, termed handles, are placed at designated positions on the surface of DNA nanotubes with nanometer precision to host a myriad of fluorophores. In this work, handles (see **Table S1** for sequences) are precisely positioned at 42 bp or ~14 nm apart on each helix to maximize labeling density while minimizing self-quenching. As such, each 6hb structure can accommodate up to 100 copies of fluorophores of interest (e.g., monomeric enhanced green fluorescent protein, mEGFP) in the center, with 12 additional handles at each end reserved for other fluorophores with distinct emission spectra (e.g., Alexa Fluor 647) to aid focusing and quality control. Additionally, 4

handles are evenly spaced on one of the helices to display biotin labels for surface attachment. We designed five versions of 6hb structures to carry 5, 25, 50, 70, and 100 mEGFPs (**Figure 2a**), which we prepared from a 7308-nt long circular ssDNA and 5 different pools of synthetic oligonucleotides following well-established DNA-origami assembly and purification protocols. (Bellot et al., 2013; Douglas, Dietz, et al., 2009; Lin et al., 2013; Stahl et al., 2014; Wagenbauer et al., 2017)

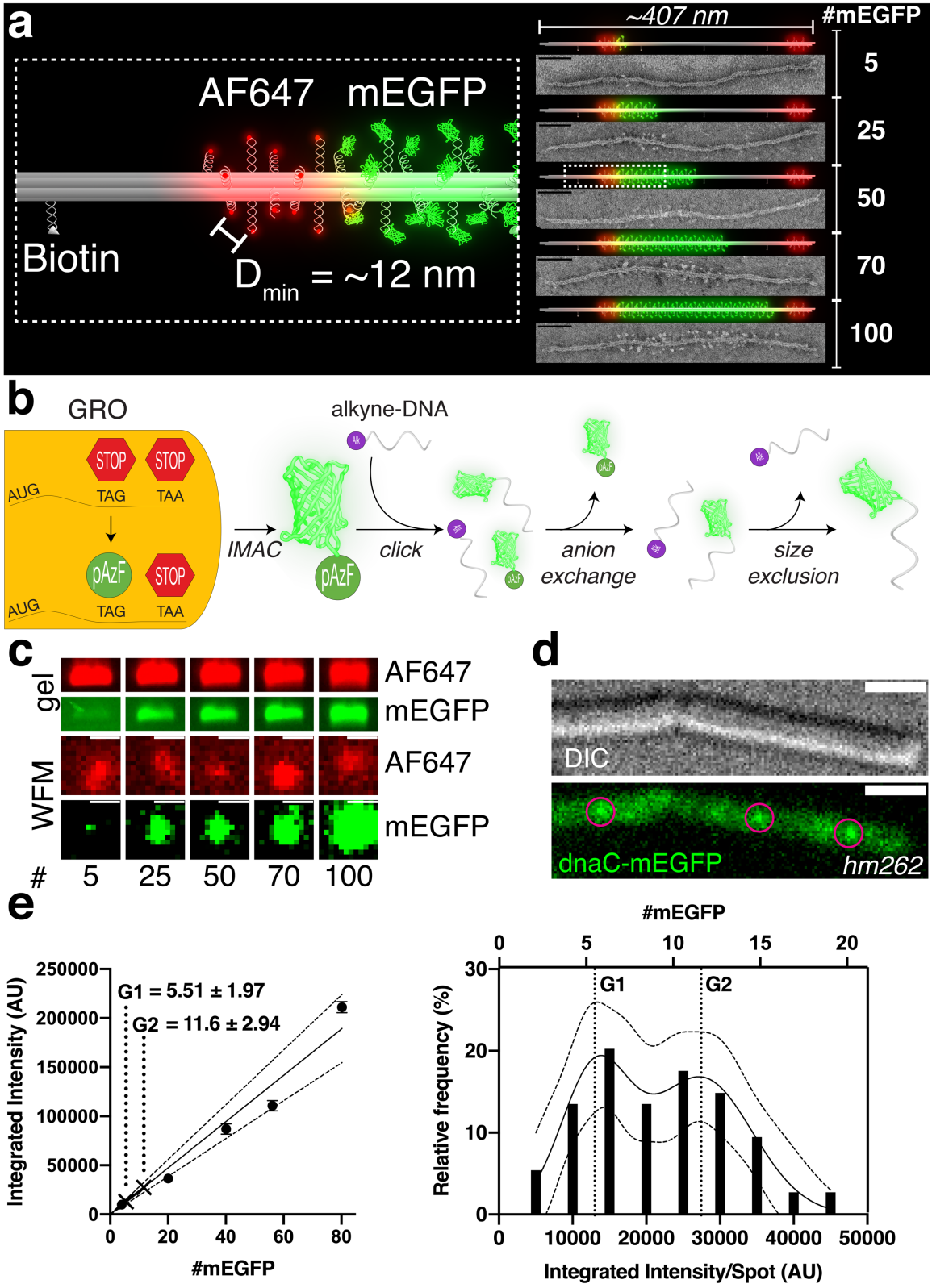
a
AF647
mEGFP
Biotin
D min = ~12 nm
~407 nm
#mEGFP
5
25
50
70
100
b
GRO
STOP
STOP
AUG
TAG
TAA
pAzF
STOP
AUG
TAG
TAA
alkyne-DNA
IMAC
click
anion exchange
size exclusion
c
gel
AF647
mEGFP
WFM
AF647
mEGFP
#
5
25
50
70
100
d
DIC
dnaC-mEGFP
hm262
e
Integrated Intensity (AU)
G1 = 5.51 ± 1.97
G2 = 11.6 ± 2.94
#mEGFP
Relative frequency (%)
G1
G2
Integrated Intensity/Spot (AU)

Figure 2. A DNA-origami-based mEGFP brightness standard.
(a) 3D models and TEM micrographs of monomeric DNA 6hb structures labeled with 5–100 copies of mEGFP (green) in the main body, 12 copies of Alexa Fluor 647 (red) at each end, and 4 biotin molecules along one side. The minimum spacing of the fluorophores is ~12 nm. Scale bars: 50 nm. (b) Generation of mEGFP-DNA conjugate. mEGFP-pAzF is expressed and purified from a GRO, in which the antisense TAG codon has been reassigned to encode pAzF, an azide-modified Phe. mEGFP(pAzF) was purified *via* immobilized metal affinity chromatography (IMAC), then reacted with alkyne-labeled DNA. Two subsequent purification steps removed unreacted proteins and DNA. (c) Gel electrophoresis (top) and widefield microscopy images (WFM, bottom) of mEGFP standards. Images are set to the same brightness scale (no saturated pixels in the original images). Scale bars: 2 μm. (d) Differential interference contrast (DIC, top) and WFM (bottom) images of *B. subtilis* (strain NW001) expressing dnaC-mEGFP. Circles indicate puncta picked for quantification. Scale bars: 2 μm. (e) Quantifying dnaC-mEGFP. Left: a calibration curve with intensities of DNA-origami standards and interpolated protein counts (mean±SEM) from dnaC-mEGFP puncta. Dotted lines denote 95% confidence interval. Right: frequency distribution and sum-of-two-Gaussians fit of dnaC-mEGFP puncta.

2.2 Generation of DNA-mEGFP Conjugates

To generate DNA-conjugated mEGFP, we used a Genomically Recoded Organism (GRO) to express mEGFP with a single azide-bearing nonstandard amino acid, p-azidophenylalanine (pAzF), at the C-terminus (Amiram et al., 2015; Lajoie et al., 2013). This was subsequently conjugated to an alkyne-labeled DNA oligonucleotide with complementary sequence to the handles (termed antihandles) by copper-mediated azide/alkyne click chemistry. The conjugation product was purified by anion-exchange and size-exclusion chromatography in two consecutive steps (**Figure 2b** & **S5**–**S8**, see online methods). This conjugation method has advantages compared to conventional crosslinking chemistry such as thiol-maleimide, amine-NHS ester, or SNAP-benzylguanine, in that it cleanly allows 1:1 DNA-protein conjugation with a site-specific, single amino-acid addition that keeps the protein structure and biochemistry

perturbation to a minimum. Further, it may be applied to any protein expressed by such GROs using readily available chemicals in aqueous solutions, allowing the creation of imaging standards with any fluorescent protein. The purified mEGFP-antihandle conjugate was then hybridized to the 6hb structures bearing 5–100 handles to generate desired mEGFP standards, which were purified by polyethylene glycol fractionation (Shaw et al., 2015).

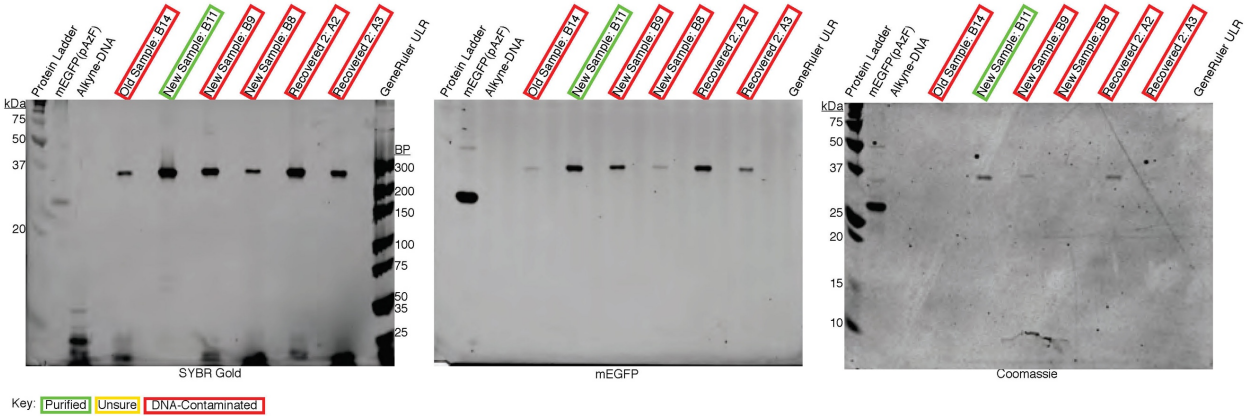

Figure 3. Purified mEGFP-DNA conjugates.

Neither unreacted mEGFP(pAzF) nor alkyne DNA were found in purified fractions (B11).

2.3 Quality Control of mEGFP Standards

These mEGFP-labeled structures were first characterized by a quantitative electrophoresis analysis. Each structure's band mobility corresponded well to the designed numbers of mEGFP per structure, with band intensities increasing proportionally to the number of fluorophores (**Figure 2c** & **Figure 4**), showing no evidence of mEGFP self-quenching (**Figure 5**). Negative-stain TEM imaging produced striking micrographs of these decorated structures (**Figure 2a** & **S8**) that further confirmed the expected mEGFP density and location on the 6hb tubes. In order to

normalize for sub-stoichiometric labeling of DNA-origami structures, stepwise photobleaching was performed on a 6hb tube designed to carry 5 molecules of Alexa Fluor 488. Fitting the step counts to a binomial distribution yielded the fluorophore attachment probability of ~0.80 (**Figure 6**); e.g., 100× mEGFP standard had an average of 80 fluorescent proteins, 70× standard had 56, and so on. The labeling efficiency we measured is consistent with previous reports (Acuna et al., 2012; Schmied et al., 2012).

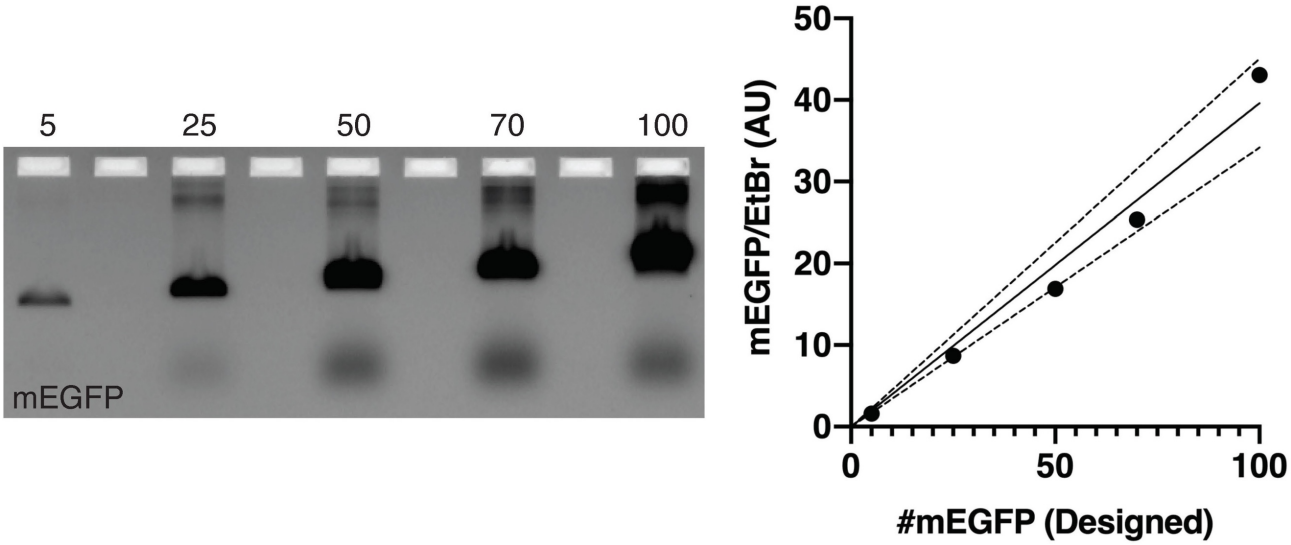

Figure 4. Intensity Increases Linearly with #mEGFP
DNA nanotubes designed to accommodate 5–100 mEGFP were labeled with mEGFP-antihandles and run in a non-denaturing agarose gel (left). After the mEGFP channel (488 nm) was imaged, the gel was stained with 0.5 µg/mL EtBr and imaged again (532 nm). The band intensities were quantified using ImageQuant TL, and normalized mEGFP fluorescence was plotted (right). A standard linear regression GraphPad Prism (8.4.3). (2020). [MacOS]. GraphPad Software) yielded a slope of 0.3962 (solid line) with a 95% confidence interval (CI) of 0.3417 to 0.4508 (dashed lines).

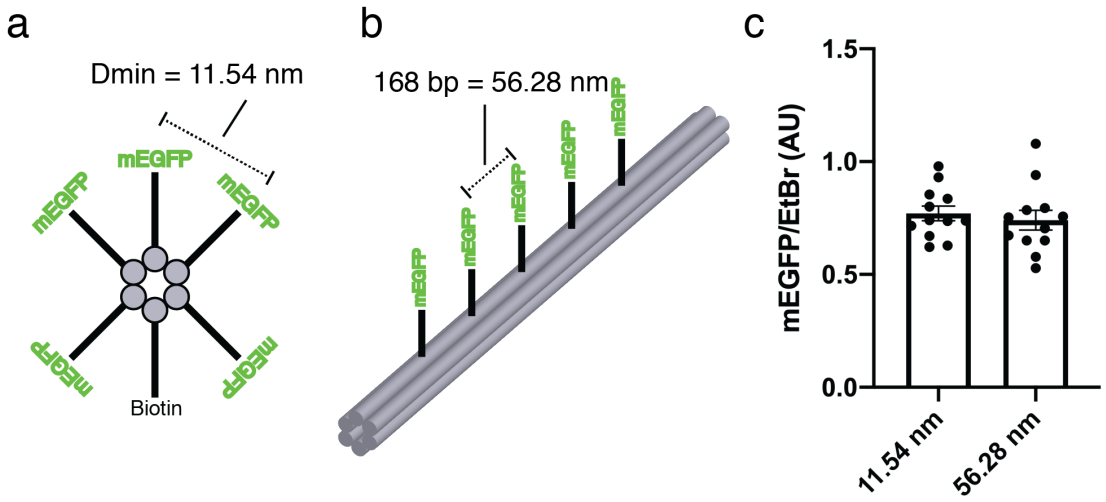

Figure 5. Test for mEGFP Self-Quenching

6 Structures were designed to host 5× mEGFPs, 3 with the same inter-protein distances as the rest of this work (a), and 3 had mEGFP placed every ~56 nm (b). In each structure, unique handle locations were chosen to negate the influence of specific handle incorporation efficiencies. All 6 structures were run in quadruplicate in a non-denaturing agarose gel and imaged before and after EtBr staining. Normalized mEGFP band intensities were nearly identical, regardless of spacing (mean±SEM), showing no sign of self-quenching.

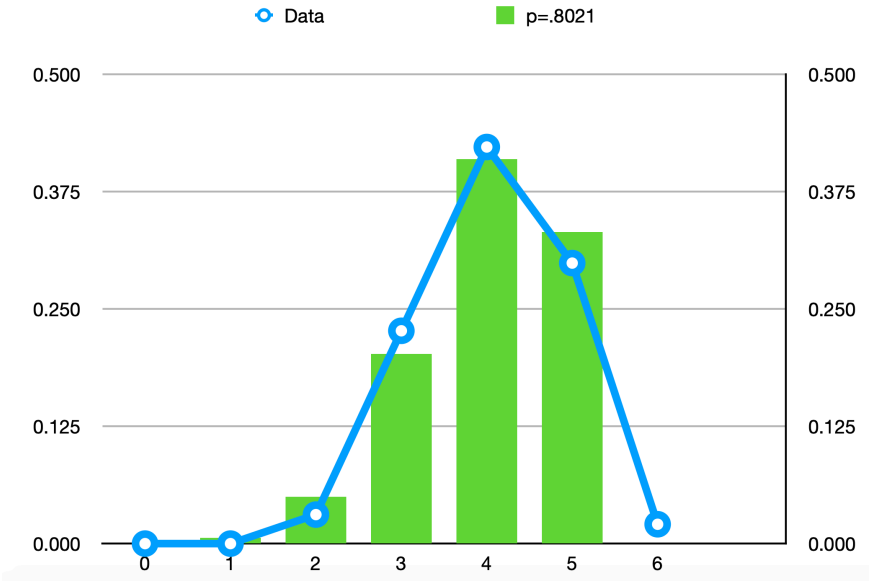

Figure 6. Handle Occupancy Estimation

Structures designed to host 5× mEGFP were labeled with Alexa Fluor 488-labeled antihandles and imaged on a Nikon TIRF microscope until fully bleached. The total photobleaching steps of the fluorescence traces were fit to a binomial function with MATLAB (The MathWorks MATLAB, 2020). The best fit probability was p=0.8021, 95% CI = [0.7634 0.8370]. Note: 2 out of 97 traces showed 6 apparent steps, and were excluded from the binomial fit.

2.4 Quantification of DnaC in live *B. subtilis* cells

To demonstrate the utility of our origami-based brightness standards, we used them to quantify dnaC in *B. subtilis*. DnaC is a well-studied helicase that has been shown to assemble into a homo-hexameric ring at the replication fork (Bailey et al., 2007; Fass et al., 1999; Kaplan et al., 2013; Mangiameli et al., n.d.). Because bacteria contain a single chromosome with two replication forks, dnaC-mEGFP puncta should appear to have 6 or 12 monomeric dnaC, depending on the proximity of the replication forks (Mangiameli et al., n.d.). Cells expressing dnaC-mEGFP and each of the origami standards were immobilized on separate agar pads and imaged with a widefield fluorescence microscope under the same conditions. After subtracting background fluorescence from agar pads and cell autofluorescence, spots were then picked using the ImageJ plugin MicrobeJ (Ducret et al., 2016) (**Figure 2c–e, Figure 7, S9**-10). To reduce imaging artifacts, we selected only DNA-origami spots that coincided with slightly elongated Alexa Fluor 647 spots, and dnaC spots that resided within the rod-shaped cells. Spots from origami structures were used to create a standard curve correlating fluorescence intensity to molecule number, which showed excellent linearity (**Figure 2e**), similar to the bulk measurement by gel electrophoresis (**Figure 4**). The variance of brightness from the standard structure is consistent with the heterogeneity of fluorescent output of mEGFP molecules (Tsien, 1998) and mEGFP labeling efficiency. Finally, the distribution of intensities from bacterial mEGFP puncta were fit to a sum of two Gaussians and calibrated against the standard curve to derive the dnaC stoichiometry. Our method resulted in 5.50±1.97 and 11.6±2.94 (mean±SD) dnaC per puncta (**Figure 2e**), which

agrees well with the expected dnaC counts of 6 and 12 molecules (Mangiameli et al., n.d.).

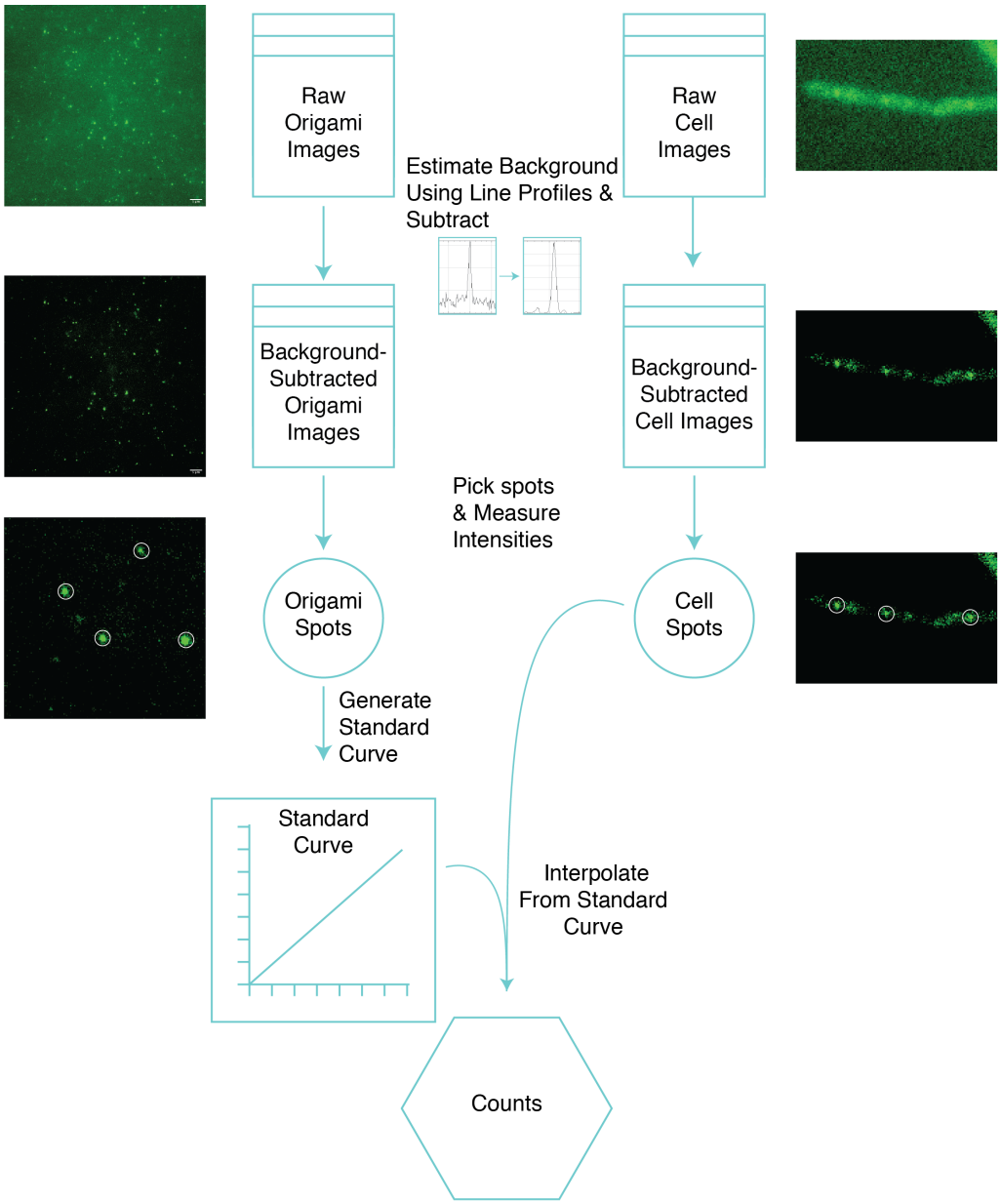

Figure 7. Image processing pipeline for mEGFP labeling.
Background fluorescence from agar pads and cell auto-fluorescence was estimated by measuring line profiles spanning cells and DNA-origami standards, then subtracted from the image. Spots were picked using MicrobeJ (Ducret et al., 2016), and were subsequently selected manually (see Materials and Methods for criteria). These intensities were fit to a sum of two Gaussians function using GraphPad Prism (GraphPad Prism (8.4.3). (2020). [MacOS]. GraphPad Software).

Chapter 3: SiR Standard

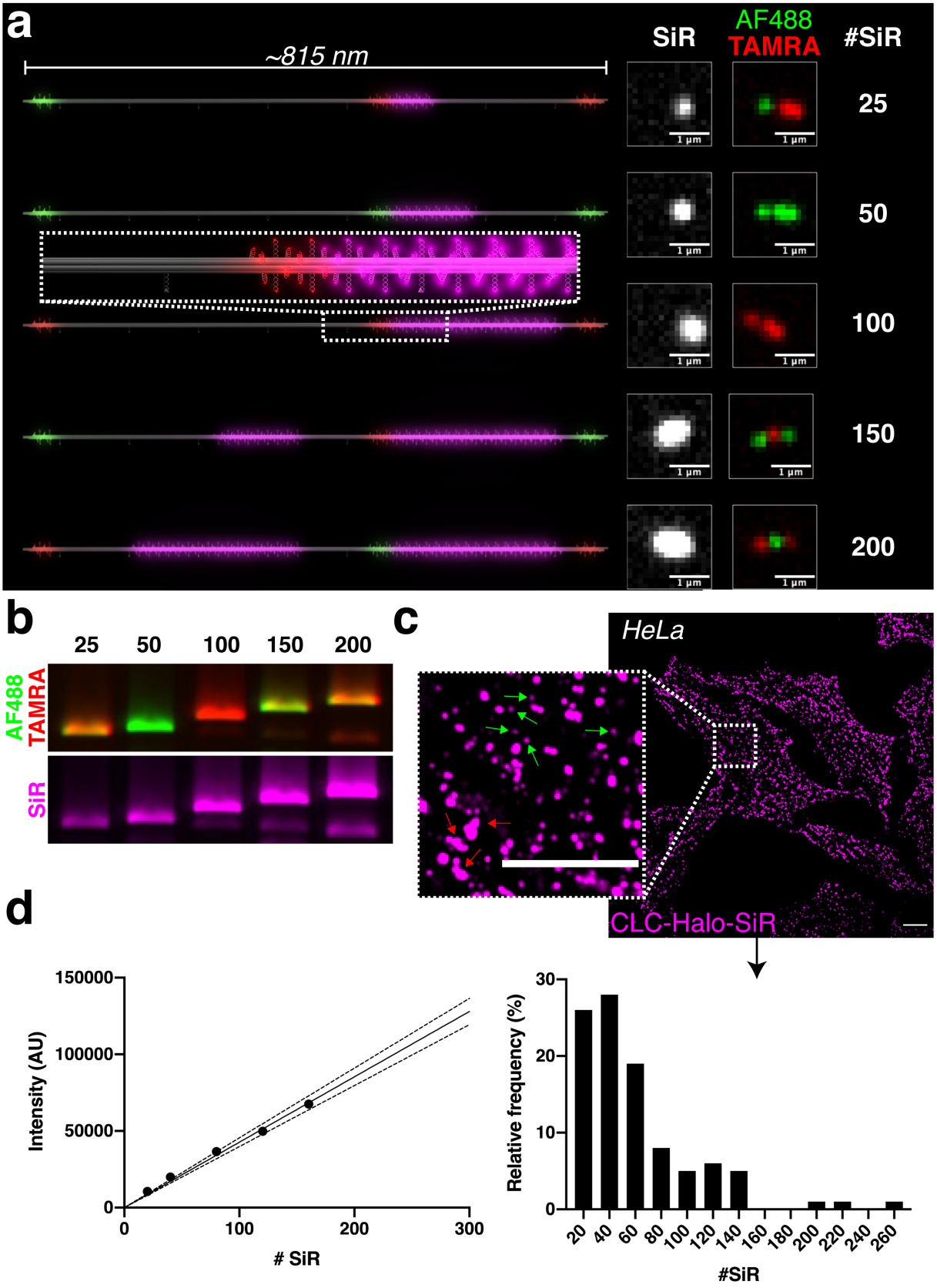

Figure 8. A DNA-origami-based SiR brightness standard.
A DNA-origami-based SiR brightness standard. (a) 3D models of dimeric DNA-origami nanotubes hosting 25–200 SiR molecules (magenta) in the main body, as well as Alexa Fluor 488 (Green) and TAMRA (red) at three distinct locations (12 fluorophores at each location) for barcoding. Confocal microscopy images revealed the expected barcoding patterns and corresponding increase in SiR intensity. Scale bars: 1 μm. (b) Agarose gel images of SiR standards show the expected combinations of barcoding dyes Alexa Fluor 488 and TAMRA, as well as increasing SiR intensity. (c) Confocal images of HeLa cells expressing Halo-fused clathrin light chain (CLC) after labeling with SiR-chloroalkane. Inset shows details of coated pits (small and round, green arrows) and plaques (larger and irregularly shaped, red arrows). Scale bars: 10 μm. (d) Quantifying SiR-labeled CLCs. Left: Calibration curve generated from DNA-origami-based SiR standards (SEM too small to see). Dotted lines denote 95% confidence interval. Right: Spots containing SiR-labeled CLCs binned by molecule number.

3.1 Expanding our Method's Reach

In addition to quantifying widefield images of GFP-tagged protein in bacteria, we sought to demonstrate our system's broad applications by counting dye-tagged clathrin light chain (CLC) molecules in mammalian cells using confocal microscopy (**Figure 8**). During receptor-mediated endocytosis, CLC molecules assemble with adaptors and other regulatory proteins into clathrin-coated pits and plaques, distinguished by size, clathrin number, and dynamics (Saffarian et al., 2009; Sochacki & Taraska, 2019). Coated pits are smaller and more circular than plaques, making it relatively straightforward to distinguish between the two in micrographs. Coated pits assemble into clathrin cages containing varying numbers of triskelia, each comprised of 3 clathrin heavy chains and 3 clathrin light chains (Harris & Marles-Wright, 2017). The reported numbers of CLCs in a single vesicle vary widely between different tissues and methods of estimation (Ehrlich et al., 2004; Kirchhausen et al., 2014; Otter et al., 2010; Sochacki & Taraska, 2019). The recruitment, assembly and disassembly of membrane-coating

clathrin structures are highly dynamic (~28–200-s life-time; 35–100 triskelia, or ~100–300 CLCs, for a mature clathrin-coated endocytic pit or vesicle) (Cheng et al., 2007; Ehrlich et al., 2004; Lehmann et al., 2019).

3.2 Design Additions

To accommodate more fluorophores, we built dimeric 6hb nanotube structures (**Figure S4** and **Table S2**) that can in theory host up to ~300 fluorophores (though a maximum of 200 were used in this study). The dimeric nanotube is designed to have 3 barcoding zones reserved for Alexa Fluor 488 or TAMRA (12 fluorophores per zone) to enable the selection of intact dimer structures and, potentially, sorting after simultaneous acquisition (Lin et al., 2012) (**Figure 7a**). To quantify Halo-tagged CLC labeled with far-red dye silicon rhodamine (SiR) (Lukinavičius et al., 2013; Thompson et al., 2017) in live HeLa cells, we labeled our fluorescent standards with the same dye. Similar to the mEGFP-DNA conjugation, SiR-azide was conjugated to alkyne-DNA *via* copper-mediated click chemistry (Amiram et al., 2015; El-Sagheer & Brown, 2010; Presolski et al., 2011) and then purified using denaturing polyacrylamide gel electrophoresis (PAGE) (**Figure S11**, also see online methods).

3.3 Quality Control of SiR Standards

Upon hybridizing SiR-labeled anti-handles to the DNA nanotubes, we analyzed the SiR-labeled standards using agarose gel electrophoresis, which showed SiR intensity increasing linearly with the designed dye numbers and the expected barcoding dye combinations (**Figure 8b**). The biotinylated SiR standards were then purified by rate-

zonal centrifugation, individually immobilized on streptavidin-coated glass-bottom dishes, and imaged under confocal microscope (**Figure 8a** & **S12**–17), which confirmed high-quality dimeric structures by fluorescent barcode patterns.

3.4 Quantification of CLC-Halo in Live HeLa Cells

Next, we applied these standards to counting SiR-labeled CLCs near the surface-adhering membranes of live HeLa cells (**Figure 8c**–**d, S18**). Cells and standards were imaged on the same day under identical conditions, and SiR-fluorescent spots were selected from the background-subtracted images using a custom TrackMate (Tinevez et al., 2017) script (**Figure 8d**, left & **Figure 9**). SiR puncta in HeLa cells were manually picked to identify those resembling clathrin-coated pits (round-shaped puncta < ~1 μm^2), and CLC counts per cluster were quantified using our DNA-origami calibration curve (**Figure 8d**, right). Out of the 100 clusters, 97 of them contain no more than 150 CLC (median = 47.8), with a decreasing frequency as molecule number increased. We note that although this pattern of distribution is to be expected from clathrin cages that pinch off shortly after completing assembly (Ehrlich et al., 2004; Sochacki & Taraska, 2019), the CLC counts per cluster obtained here are significantly smaller than those previously reported for clathrin-coated vesicles (typically ~100–240 CLCs for vesicles 30–50 nm in diameter) (Cheng et al., 2007). However, this is likely because of the less-than-perfect SiR-labeling efficiency in cells and oversampling of short-lived, abortive clathrin clusters that contain fewer CLCs (Ehrlich et al., 2004; Lehmann et al., 2019).

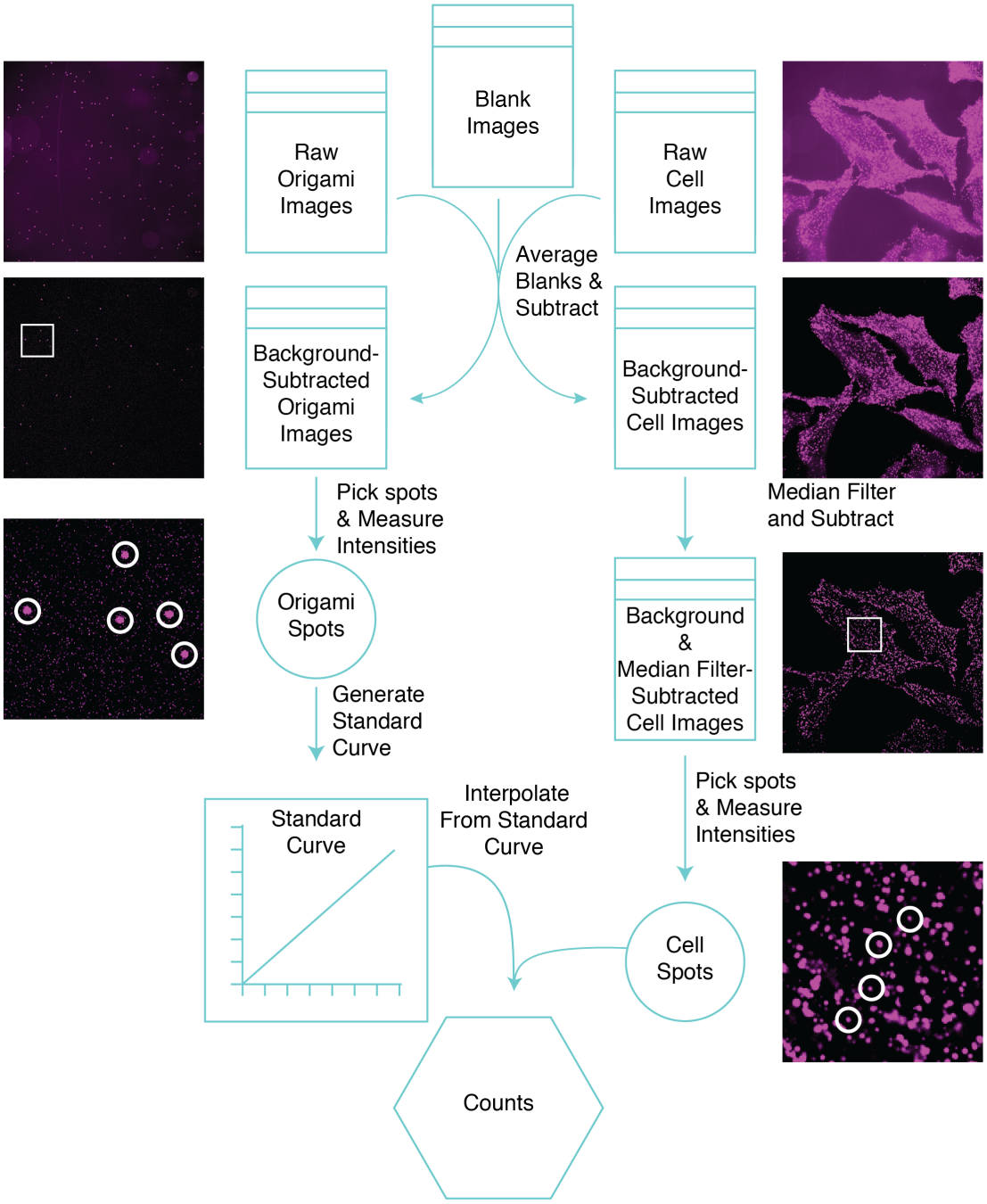

Figure 9. Image processing pipeline for SiR labeling.
Background from media and the dish was approximated from empty dishes (blank images), and subtracted from all images containing SiR standards or HeLa cells. SiR puncta in DNA-origami images were picked using a custom TrackMate script, and used to construct the calibration curve. A background-subtracted image of cells was median filtered, and was subtracted from the cell images. CLC-SiR spots in cells were then picked manually (circled in sample images). CLC-SiR intensities were then converted to molecule number using the calibration curve.

Chapter 4: Discussion

4.1 System Strengths

In summary, our DNA-origami-based brightness standards provide a versatile, easy-to-implement system for quantifying 5–300 clustered proteins using fluorescence microscopes readily accessible to cell biology labs. The most valuable features of our standards are their programmability to accommodate fluorophores of various types and stoichiometry, their robustness to withstand near-physiological conditions (**Figure S25**) (Kielar et al., 2018), and their low entry barrier to use without specialized equipment or software. Typically, imaging these standards adds less than 2 hours to a typical cell imaging session (compared to several days using alternative methods), and thus can be easily integrated into biologists' conventional workflows to obtain very good estimates of protein counts. While we demonstrate the standards' application in bacteria and mammalian cells, they should, in principle, be compatible with any cell type. Similarly, because of the large library of DNA-fluorophore conjugation chemistry (Yang et al., 2015), including our GRO-enabled protein conjugation, our system can be used to display and count practically any fluorophore. The wide selection of fluorescent dyes, combined with the barcoding capability of the DNA-origami structures (**Figure S19**), open up opportunities for multiplexed imaging. Moreover, with the right combination of fluorophore, protein-labeling technique, cellular context, microscope system and imaging conditions, it is possible to quantify as few as a single fluorophore (Xia et al., 2013), as well as to increase the upper limit of the dynamic range beyond 300, *via* additional 6hb multimerization.

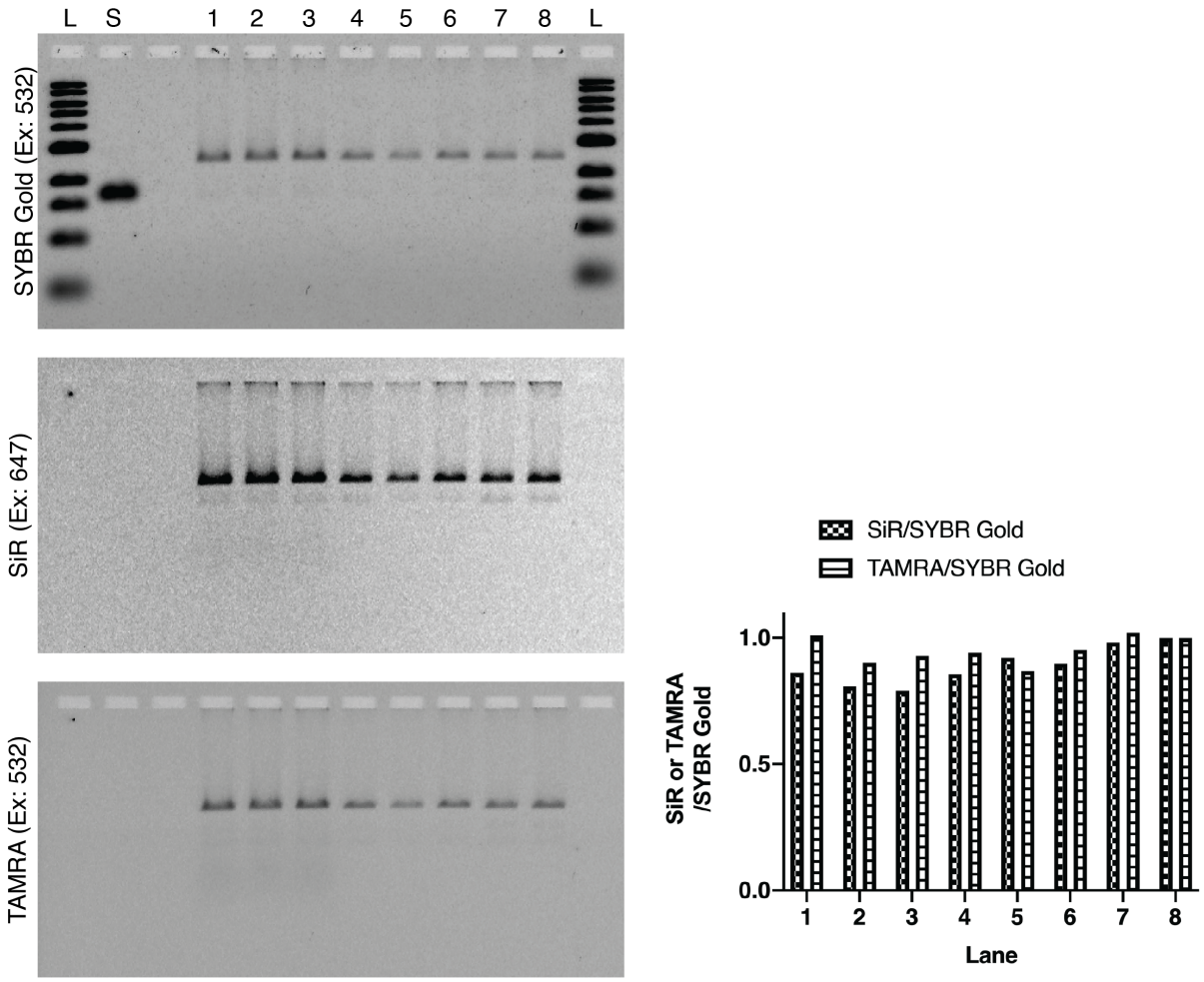

Figure 10. Stability of DNA-origami standards in imaging media.
A dimeric-6hb-based SiR standard bearing 20 copies of SiR and 36 copies of TAMRA were subjected to media and temperatures simulating live-cell imaging conditions and run on an agarose gel. The media and temperature conditions were as follows: 1: Regular DMEM (Gibco, 21063-029, contains ~1 mM Mg^{2+}), 1hr @ 37°C; 2: DMEM + 2 mM $MgCl_2$, 1hr @ 37°C; 3: DMEM + 10 mM $MgCl_2$, 1hr @ 37°C; 4: Regular LCIS (Thermo Fisher, pH 7.4, A14291DJ, contains ~1 mM Mg^{2+}), 1hr @ 37°C; 5: LCIS + 2 mM $MgCl_2$, 1hr @ 37°C; 6: LCIS + 10 mM $MgCl_2$, 1hr @ 37°C; 7: 1×TE + 10 mM $MgCl_2$, 1hr @ 37°C; 8: 1×TE + 10 mM $MgCl_2$, RT (reference). SiR, TAMRA, and SYBR Gold intensities were measured using ImageJ and the ratios of SiR and TAMRA to SYBR gold are shown on the right (bar chart normalized to lane 8). Importantly, there was no indication of structural damage or fluorescence loss in LCIS or DMEM, no matter the concentration of Mg^{2+} (1–10 mM), or whether structures were heated to 37ºC, supporting the reliability of our DNA-origami brightness standards under live-cell imaging conditions.

4.2 System Limitations and Future Directions

The primary limitation of our system is that the standards are external to the cell, and so must be imaged in media similar to the cellular compartment being studied. Because the main media effectors of fluorescence output are solvent polarity and pH (Mahon, 2011; Miesenböck et al., 1998; Papkovsky, 2009; Straight, 2007), this obstacle can be overcome by matching the pH of the aqueous imaging media to the cellular pH, as is the case in *HeLa* and *B. subtilis* cytosol (Beilen & Brul, 2013; Llopis et al., 1998). In cases where the cellular pH is unknown or dynamic, our universal conjugation method allows attachment of pH-sensitive fluorophores like pHluorin (Mahon, 2011; Miesenböck et al., 1998) to account for any pH differences. In this work, we used a few existing, commonly used image-analysis software to extract quantitative data from micrographs. However, we envision that a specialized particle-tracking and pattern-recognition software, perhaps with future development of machine learning, will further expedite the workflow. Indeed, with the programmable DNA-origami platform and the fast-evolving microscopy techniques, the potential applications of DNA-origami-based quantitative microscopy (see **Table 1)** for brief summary) are endless.

Table 1. DNA-Origami-assisted quantitative fluorescence microscopy methods

	DNA-origami-based brightness standards		DNA-origami-calibrated STORM	DNA-PAINT-based quantification
Reference	18,19,20	This work	21	22,23
Dynamic range	1-132	5-200	1-35	1-50
Speed	Fast		Slow	Slow
Fluorophore and conjugation	DNA-conjugated cell-impermeable organic dyes	Fluorescent proteins and cell-permeable organic dyes	Antibody-conjugated organic dyes	DNA-conjugated organic dyes
Biological sample?	No	Live cells	Fixed cells	Fixed cells: require antibody-conjugated DNA strands
Difficulty	Low	Low	High	High
Acquisition time	Typically <1 sec	1 sec	~1 hour	0.4-2.8 hours

Materials and Methods

Materials

DNA oligonucleotides were synthesized by Integrated DNA Technologies. All chemical reagents were purchased from Millipore Sigma unless otherwise specified. Enzymes were purchased from New England Biolabs unless otherwise specified. Water is purified by a Milli-Q (Millipore) system.

Agarose gel electrophoresis

Unless otherwise indicated, all agarose gels contained 1.5% agarose, and were run in 0.5×TBE + 10 mM $MgCl_2$ for 3 hrs at 5V/cm at room temperature. Gels were imaged on a Typhoon FLA 9500 scanner. Whenever necessary, gels were stained with Ethidium Bromide (EtBr, 0.5 μg/mL) after imaging any other relevant channels (for fluorescent labels on DNA-origami structures).

SDS-polyacrylamide gel electrophoresis (SDS-PAGE)

Unless otherwise indicated, all gels contained 12% acrylamide bis-tris (Bio-Rad), and were run for 45 minutes at 200 V in 1× SDS MOPS buffer (50 mM Tris base, 50 mM MOPS, 1 mM EDTA, 0.1% SDS, pH 6.5). Samples were prepared in 30% glycerol supplemented with orange G dye, and were heated 5 minutes at 95ºC before loading. In gels where mEGFP was imaged, SDS was first rinsed away by three 20-minute washes in water. We found this protocol was able to recover mEGFP fluorescence sufficiently to image (See Figure S5).

SYBR Gold staining was performed by submerging gels in SYBR Gold stain (Invitrogen) diluted 10,000× in water, per manufacturer recommendations. Gels were briefly rinsed with water before imaging on a Typhoon FLA 9500 scanner.

Coomassie staining was performed by submerging gels in 1× Coomassie solution (50% methanol, 10% glacial acetic acid, 0.1% w/v Coomassie blue) and microwaving on high until boiling (approximately 1 minute). Gels were then briefly rinsed with water, covered in Coomassie destain solution (12% methanol, 7% glacial acetic acid), and microwaved on high until boiling (approximately 1 minute). Containers with gels heated in destain solution were then placed on a platform shaker, and Kimwipes were added to speed Coomassie desorption. Gels were checked approximately every 30 minutes until clear enough to be imaged. Coomassie-stained gels were imaged on a transilluminator (Bio-Rad) with white light. In cases where multiple scans were used, gels were imaged and stained in the following order: in-gel fluorophores (e.g. mEGFP), SYBR Gold, and Coomassie.

DNA-origami structure design

DNA-origami six-helix bundle (6hb) nanotubes were designed using caDNAno (cadnano.org) (Douglas, Marblestone, et al., 2009). Design diagrams are shown in Figure S4. Orthogonal handle sequences were generated using NUPACK (nupack.org) and added to the 3'-ends of selected staple strands. Handle sequences are shown in Table S1.

DNA-origami structure folding and purification

DNA origami folding mixtures were prepared by adding 6× molar excess of staple strands to p7308 scaffold (Douglas, Dietz, et al., 2009) in 1×TE buffer (25 mM Tris•HCl, 1 mM EDTA•Na_2, pH 8) supplemented with 10 mM $MgCl_2$. Mixtures were heated in a thermocycler (Bio-Rad) to 85ºC for 3 min, cooled from 80ºC to 60ºC in 80 minutes, 60ºC to 24ºC in 15 hours, and then held at 4ºC. Excess staples were removed by PEG precipitation and re-suspending pellets in 1×TE buffer + 10 mM $MgCl_2$ (Stahl et al., 2014).

DNA-origami structure dimerization

“Front” and “rear” monomeric halves of dimeric nanotubes were folded independently and PEG precipitated to remove excess staples (see above). Concentrations of purified monomers were estimated by absorbance, and equimolar amounts of each half were mixed in 1×TE buffer + 10 mM $MgCl_2$ with 10× molar excess of linker strands (Table S2). These dimer mixtures were heated to 55ºC and cooled to 20ºC over 18 hours.

Fluorescently labeling DNA-origami structures

To add antihandles to DNA nanotubes, a molar excess of antihandle was added to origami in 1×TE buffer + 10 mM $MgCl_2$: 3× excess for mEGFP and SiR antihandles, and 1.2× excess in the case of other antihandles. 3× excess was used to maximize antihandle attachment for the most important fluorophores. The mixture is incubated at 37ºC for 2 hours. In the case of dimeric structures, linker DNA was kept at 10× molar excess during the labeling step. The labeled DNA-origami dimers were then purified by rate-zonal centrifugation (see below).

mEGFP standard purification

DNA-origami nanotubes labeled by mEGFP and Alexa Fluor 647 were PEG precipitated to remove excess antihandles. Briefly, a equal volume of 2×PEG-precipitation buffer (1×TE, 15% PEG, 10 mM $MgCl_2$, 500 mM NaCl, pH 8) was added to the hybridization mixture (DNA nanotubes + labeled-antihandles), and the mixture was spun at 16,000-g for 25 minutes at 4°C. The pellet was then resuspended in 1×TE + 10 mM $MgCl_2$. A typical preparation starting with 45 μL of 4 nM unlabeled DNA nanotubes yields 45 μL of 2.7 nM purified mEGFP-labeled DNA nanotubes, over 67% recovery.

Transmission electron microscopy

For negative-stain TEM, a drop of the sample (5 μL) was deposited on a glow discharged formvar/carbon-coated copper grid (Electron Microscopy Sciences), incubated for 1 min, and blotted away. The grid was first rinsed twice with 1× TE buffer + 10 mM $MgCl_2$, then washed briefly and stained for 1 min with 2% (w/v) uranyl formate. Images were acquired on a JEOL JEM-1400Plus microscope (acceleration voltage: 80 kV) with a bottom-mount 4k×3k CCD camera (Advanced Microscopy Technologies).

SiR standard purification

Dimeric DNA-origami nanotubes labeled with fluorophores and biotin were purified by rate-zonal centrifugation over a glycerol gradient (Lin et al., 2013). Gradients were 15%–45% glycerol in 1×TE buffer supplemented with 10 mM $MgCl_2$, and were spun at 48k RPM for 1.5 hrs at 4ºC. Fractions were subsequently collected and run in agarose gels to find the fractions containing properly labeled dimers. A typical preparation

starting with 90 μL of 15 nM dimeric DNA nanotubes yields 600 μL of ~1 nM purified SiR-labeled DNA nanotubes.

mEGFP-pAzF cloning

The sequence for mEGFP was cloned from plasmid pFA6a-mEGFP-kanMX6 (Addgene plasmid # 87023; RRID:Addgene_87023), and was inserted into destination vector pZE21-GFP-NHis-0TAG generated by the Isaacs lab (Lajoie et al., 2013). First, overlap-extension PCR was used to add an EcoRI restriction site and a 6×His tag to the N-terminal of mEGFP, and a TAG codon and BamHI restriction site to the C-terminus. The resulting PCR product and destination vector were both digested with EcoRI and BamHI and purified by agarose gel electrophoresis. The gel-purified products were then ligated using T4 ligase. The final plasmid introduced into the GRO contained mEGFP with a 6×His N-term tag and a C-term TAG codon with inducible expression controlled by a pLtetO promoter. DH5α cells were transformed with this plasmid and plated on kanamycin-selective agar plates. 20 colonies were picked and PCR tested with the forward and reverse primers used to clone the mEGFP insert. 4 colonies that produced the expected PCR result were grown overnight and extracted using a Miniprep kit (Qiagen). The resulting plasmid DNA was sequenced. Of the 4 sequenced colonies, 1 contained the exact 6×His-mEGFP-TAG sequence as designed. A small volume of the DH5α culture with the correct mEGFP was stored at -80ºC in 25% glycerol.

GRO transformation

Recoded E. coli ΔmutS:Zeo (Δ1prfA):tolC)tolC (Amiram et al., 2015; Lajoie et al., 2013) was transformed with the plasmid 6×His_mEGFP-TAG (see above) and orthogonal translation system plasmid pAzFRS.1.t1 (Lajoie et al., 2013), both generated by the Isaacs lab, and plated on agar containing chloramphenicol and kanamycin. A resulting colony was picked and used to grow a ~5 mL culture, ~1 mL of which was stored at -80ºC in 25% glycerol.

mEGFP-pAzF overexpression (adapted from ref X)

A 100 mL 2×YT starter culture supplemented with chloramphenicol and kanamycin was inoculated with a miniscule volume from the glycerol stock of GRO cells transformed with 6×His_mEGFP-TAG and pAzFRS.1.t1 plasmids and grown at 34ºC overnight. This starter culture was used to inoculate a 1L expression culture supplemented with chloramphenicol, kanamycin, pAzF, and arabinose. The expression culture was grown at 34ºC to confluency (OD_{600} = 0.5–0.8), and then mEGFP expression was induced with addition of anhydrotetracycline (aTc). The induced culture was grown for ~16 hours at 34ºC. Then cells were pelleted by centrifugation at 4,000× g for 15 minutes. Supernatant was discarded and cell pellets were flash frozen and stored at -80ºC.

mEGFP(pAzF) His-trap FPLC purification

Cell pellets were thawed on ice and resuspended in lysis/wash buffer (1× PBS pH 7.4 + 25 mM imidazole, supplemented with a protease inhibitor cocktail (Roche)). Resuspended cells were lysed using a homogenizer, lysate was centrifuged at 35,000 RPM for 45 minutes, and supernatant was collected and filtered using 0.45 μm filters. A

HisTrap column was conditioned with lysis/wash buffer, and then filtered lysate was circulated ~2.5× over column to bind. The column was then washed with ~3 column volumes of lysis/wash buffer, which was collected. Bound protein was then eluted with elution buffer (1× PBS pH 7.4 + 500 mM imidazole), and fractions were collected. Fractions most likely to contain the desired product were selected by reviewing the FPLC traces (absorption at 254 & 280 nm) and were run in a reducing 12% Bis-Tris SDS-PAGE gel. Fractions confirmed to contain the desired products were pooled and buffer exchanged into lysis/wash buffer using Amicon 10k filters, then purified a second time using the HisTrap column. Fractions from the second HisTrap purification were run on a SDS-PAGE gel as before to identify the best fractions, which were then pooled, buffer exchanged into 1×PBS, pH 7.4, and measured for concentration using a BCA assay (Pierce). Finally, glycerol was added to the purified mEGFP(pAzF), which was then flash-frozen and stored at -80ºC.

mEGFP – alkyne DNA conjugation and purification

Click reaction was adapted from protocols by Presolski et al., 2011. mEGFP(pAzF) was reacted with an excess of alkyne DNA (Table S1) for 1 hr at 30ºC in degassed click reaction buffer (0.1 M potassium phosphate, 0.25 mM $CuSO_4$, 1.25 mM THPTA, 5 mM aminoguanidine HCl, 5 mM sodium ascorbate, pH 7). The reaction was then quenched by adding EDTA to a final concentration of 2.5 mM. Anion exchange was then performed using Pierce Strong Anion Exchange Spin Columns following the manufacturer's directions. Fractions were collected and stored O/N at 4ºC before running on a 12% SDS-PAGE gel (Figure S6). Fractions confirmed to contain mEGFP-

DNA conjugate but not the unreacted mEGFP were buffer exchanged into 1×PBS using 10k Amicon filters before size exclusion purification. Size exclusion was performed using a Superdex 75 Increase 10/300 column (Cytiva) connected to an ÄKTA FPLC system (Cytiva), and fractions were collected and stored at 4ºC O/N before checking with SDS-PAGE (Figure S7&S8).

SiR-azide – alkyne-DNA click reaction

SiR-azide (Spirochrome) was reacted to alkyne DNA (Table S1) using the same protocol as mEGFP conjugation (above).

Urea-PAGE Purification of SiR-DNA conjugate.

SiR-DNA conjugate was mixed 1:1 with denaturing tracking dye buffer (90% formamide, 10 mM NaOH, 1 mM EDTA-Na_2, 0.1% xylene cyanole) and heated 10 minutes at 95°C. Sample was removed from heat and immediately chilled on ice before being loaded into a denaturing polyacrylamide gel (12% acrylamide, 8.3 M urea, 89 mM tris base, 89 mM boric acid, 2 mM EDTA pH 8.0). Each gel well was loaded with 20 µL of SiR-DNA conjugate at ~2 OD, and the loaded urea-PAGE gel was run in 1× TBE buffer (89 mM tris base, 89 mM boric acid, 2 mM EDTA, pH 8.0) for 2 hours at a constant current of 30 mA and at 37°C. The gel was removed from the running apparatus, wrapped in plastic, and visually inspected on a transilluminator under white light and 302 nm UV to locate the migrated SiR-DNA conjugate. The desired SiR-DNA oligonucleotide was observable as a blue band under white light and as dark shadow cast against a phosphor screen under 302 nm UV. The desired DNA band was excised with a clean razorblade. The gel

fragments containing the SiR-DNA were diced into smaller pieces and placed into Freeze 'N Squeeze filters (Bio-Rad) along with 500 µL of elution buffer (500 mM NH_4AC, 10 mM $Mg(AC)_2•(H2O)_4$, 2 mM EDTA, pH 8.0). Freeze 'N Squeeze filters containing cut gel and elution buffer were wrapped in Al foil and agitated at room temperature for 8 hours. Filters were spun at room temperature at 8,000 rpm for 6 minutes to separate eluted SiR-DNA conjugate and gel. Eluted SiR-DNA was subsequently purified of organic contaminants via extraction with butanol (using a butanol:DNA volume ratio of 2:1). The extracted aqueous layer containing the SiR-DNA was then subjected to ethanol purification: 100% ethanol was added to the SiR-DNA solution at a 2:1 (v/v) ratio, mixed thoroughly, and then chilled at -20°C for 30 minutes. The tubes were then centrifuged at 13,000 rpm for 30 minutes at 4°C to pellet the SiR-DNA. The supernatant was decanted, and the SiR-DNA pellets were washed with ice-cold 70% ethanol followed by another 13,000-rpm spin for 10 minutes. After decanting the supernatant, the SiR-DNA pellets were air-dried overnight at room temperature in dark. After drying, solid SiR-DNA pellets were either dissolved in water/buffer of choice or stored dry at -20°C. Purification of the desired SiR-DNA fragment was confirmed by subsequent urea-PAGE analysis and comparison with Ultra Low Range DNA Ladder (Invitrogen). Importantly, the entire purification protocol was performed in dim lighting conditions with foil coverings over tubes and the gel running apparatus to minimize potential photobleaching of the SiR-DNA conjugate.

Generation of *B. subtilis* cells expressing dnaC-mEGFP

B. subtilis PY79 cells expressing dnaC-mEGFP (strain NW001) was constructed using plasmid DNA and a 1-step competence method. Original plasmid (dnaC-GFPmut2) was obtained from Alan D. Grossman at MIT Department of Biology and mutated to mEGFP using QuikChange Lightning kit (Agilent) following manufacturer's instructions. Mutations were confirmed by sequencing.

Imaging of mEGFP standards and *B. subtilis* cells

mEGFP-labeled DNA nanotubes were immobilized on a coverslip as previously described (Lin et al., 2012) for quality control imaging (not shown), and on a 2% agarose pad made with 1× M9 salts medium (Gibco) and equilibrated in arabinose minimal medium (1x Spitzizen's salts (3 mM $(NH_4)_2SO_4$, 17 mM K_2HPO_4, 8 mM KH_2PO_4, 1.2 mM $Na_3C_6H_5O_7$, 0.16 mM $MgSO_4$-$(7H_2O)$, pH 7.0), 1x metals (2 mM $MgCl_2$, 0.7 mM $CaCl_2$, 0.05 mM $MnCl_2$, 1 μM $ZnCl_2$, 5 μM $FeCl_2$, 1 μg/ml thymine-HCl), 1% arabinose, 0.1% glutamic acid, 0.04 mg/ml phenylalanine, 0.04 mg/ml tryptophan, and as needed 0.12 mg/ml tryptophan) for generating calibration curves (Figure 2c & S9). Cells were prepared as previously described by Mangiameli et al., 2017, with slight modifications. Briefly, *B. Subtilis* (strain NW001) were cultured overnight in arabinose minimal medium in a shaking incubator at 30°C. Overnight cultures at an OD_{600} of 0.4–0.9 were diluted back to an OD_{600} of 0.2 and incubated again for about 2 hr until they reached approximately OD_{600} 0.4. Cells were mounted on a 2% agarose pad, which was made with 1× M9 salts medium (Gibco) and equilibrated in arabinose minimal medium, using a gene frame (Bio-Rad). Note that both cells and the mEGFP standards were re-suspended in the arabinose minimal medium containing >2 mM Mg^{2+}. We found

no evidence of degradation or loss of fluorescence when standards were incubated in imaging media containing as low as 1 mM $MgCl_2$ (Figure 10). Fluorescence microscopy was performed using a Leica DMi8 Wide-field Inverted Microscope equipped with an HC PL APO 100×DIC objective, an iXon Ultra 888 EMCCD Camera (Andor Technology) and Lumencor´s Spectra-X LED Light Engine as the source of light. Excitation light transmission was set to 50% and exposure time for GFP (λ_{EX}=470/40; λ_{EM}=500–550) was 1 sec. See Table S3 for more details. Cells were concentrated 10× by centrifugation (3300×g for 30 sec) prior to visualization. Cells were imaged at RT. Images were acquired with Leica Application Suite X, and analysis and processing were performed using the ImageJ software.

Image processing of wide-field microscopy images

Background fluorescence from agar pads and cell autofluorescence was estimated by measuring line profiles spanning cells and origami, then subtracted from the image. Spots were picked using MicrobeJ (Ducret et al., 2016), and were subsequently selected manually: DNA-origami spots in the mEGFP channel were selected if they were non-overlapping and colocalized with signal in the Alexa Fluor 647 channel; dnaC spots were selected if they were clear, round puncta within cell boundaries (2 out of 77 puncta were excluded because of their abnormally large size and intensity). These intensities were plotted as a histogram and fit to a sum of two Gaussians function using GraphPad Prism (GraphPad Prism (8.4.3). (2020). [MacOS]. GraphPad Software). The workflow is summarized in Figure S14.

CLC (Clathrin Light Chain)-HaloTag CRISPR/Cas9 gene editing

CLC-HaloTag CRISPR cells were generated by transfecting a repair template that has Halo tag and the gRNA specific to the targeted gene. The following gRNA sequence was used for the CLC genomic DNA (Gene ID 1211): 5'- GCAGATGTAGTGTTTCCACA GGG-3' (PAM sequence is underlined). This gRNA was cloned into the SpCas9 pX330 plasmid (Addgene plasmid #42230) (Cong et al., 2013) by BbSI site. The homologous repair plasmid with HaloTag was constructed by pEGFP-C1 plasmid. The right homology arm (~1 kb) was cloned into pEGFP-C1 using EcoO109I site. The left homology arm (~1 kb) was cloned with PCR fragment of HaloTag by In-Fusion HD Cloning kit (Takara Bio USA, Inc.) using AseI and BamHI cutting sites. The target sequence (PAM site) was mutagenized in the right homologous arm.

The pX330 plasmid with gRNA of CLC and the homologous repair plasmid were transfected in HeLa CCL-2 cells using Lipofectamine 3000 (Thermo Fisher). After 48hrs post-transfection, cells were selected by G418. After selection, cells were screened by single cell cloning with serial dilution protocol in 96 well plate and immunoblot.

CLC-Halo cell cultures

Halo–CLC (Takakura et al., 2017) CRISPR/Cas9 HeLa cells were cultured in Dulbecco's modified Eagle medium (DMEM) (Gibco, 21063-029) supplemented with 10% FBS. All cells were cultured at 37°C in 5% CO_2 incubator.

CLC-Halo labeling with SiR-chloroalkane (SiR-CA) in Hela cells

Cells were seeded on 35 mm glass bottom dishes (Mattek P35G-1.5-14-C) 24 hrs before imaging. On the day of imaging *Halo–CLC* expressed in cells were labelled with

5 μM near far-red silicon rhodamine (SiR): SiR-chlroroalkane (a gift from Promega) for 30 min at 37°C. Subsequently the cells were washed three times and placed back in 37°C incubator for 1 hr.

Imaging SiR standards and SiR labeled CLC-Halo in HeLa cells

SiR-labeled DNA nanotube dimers were immobilized on a Mattek dish as previously described (Lin et al., 2012), in Live Cell Imaging Solution (LCIS) (Thermo Fisher, pH 7.4, A14291DJ). We found no evidence of degradation or loss of fluorescence when standards were incubated in imaging media containing as low as 1 mM $MgCl_2$ (Figure 10). The cells were imaged live in LCIS on TiE inverted Nikon spinning disc confocal microscope, using a 100× 1.45 Oil objective. SiR labels were imaged using a 647 nm laser line (190 mW, measured at the fiber tip) using Nikon's Perfect Focus System. See Table S3 for more details. Laser power was maintained constant throughout the imaging session after adjusting to avoid saturation. Several images of glass bottom dishes without cells were also captured at the same focal point for background correction post acquisition (see below).

Image processing of confocal micrographs

First, background from media and the cell dish was approximated by averaging 10 images of empty dishes to generate a new image. This image was then subtracted from all images containing DNA-origami nanotubes or HeLa cells. SiR puncta in DNA-origami images were picked using a custom TrackMate script (Do_subpixel_localization: True, Radius: 0.8, Threshold: 6.0, and Do_median_filtering: False), and used to construct the

calibration curve (Figure 7d). A background-subtracted image of cells was median filtered (20 px radius) to generate the approximate background intensity from cell autofluorescence and nonspecific SiR-CA labeling. This image was then subtracted from the image of cells. CLC-SiR spots in cells were then picked manually by size and morphology. Only spots that were well-defined, nonoverlapping, in-focus, and circular, were selected. These criteria were selected based on the morphological differences between coated pits and plaques previously described (Saffarian et al., 2009). CLC-SiR intensities were then converted to molecule number using the calibration curve. The workflow is summarized in Figure S24.

Appendix: Supplementary Figures & Tables

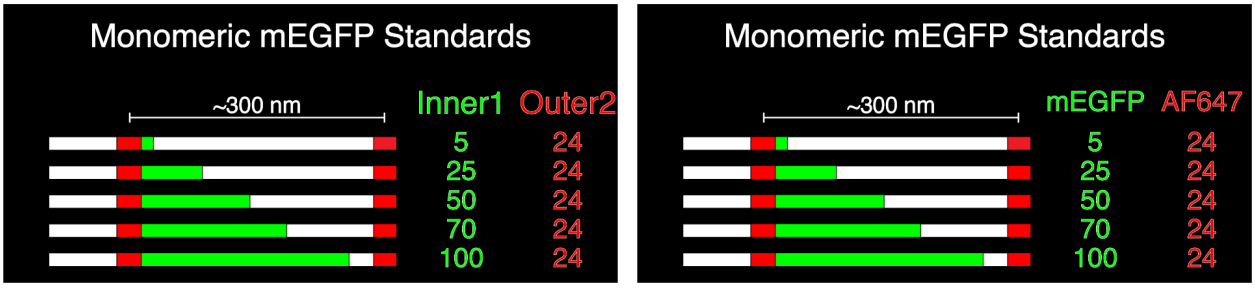

Figure S1. Diagrams of mEGFP standards.
Left: number and names of handle sequences. Right: number and names of fluorophores.

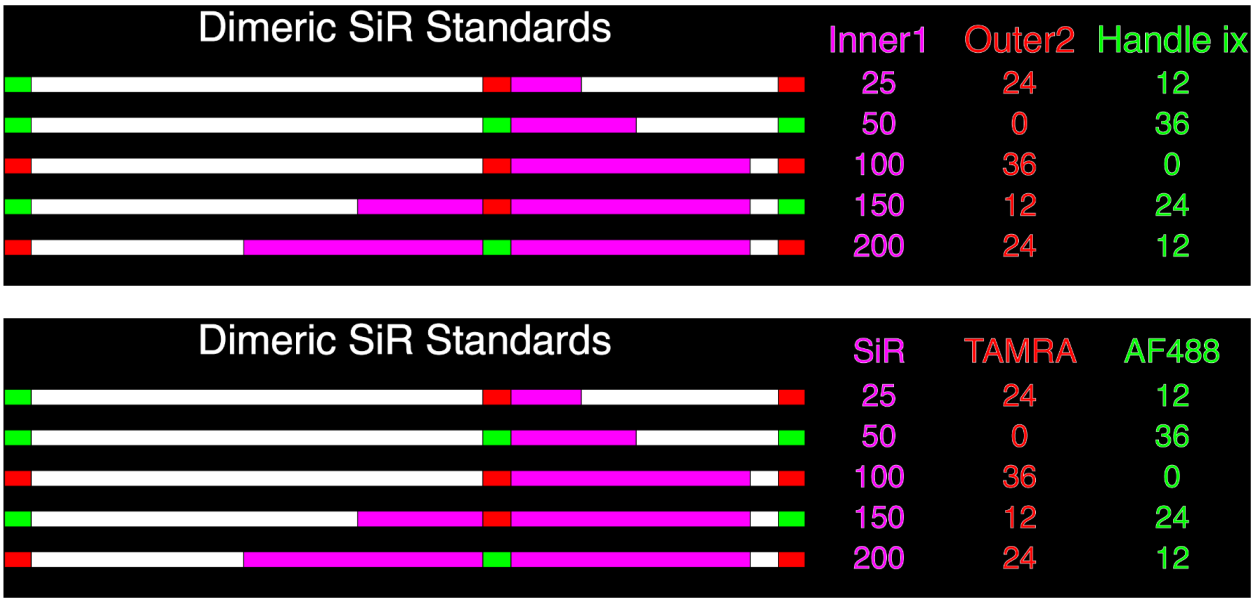

Figure S2. Diagrams of SiR standards.
Top: number and names of handle sequences. Bottom: number and names of fluorophores.

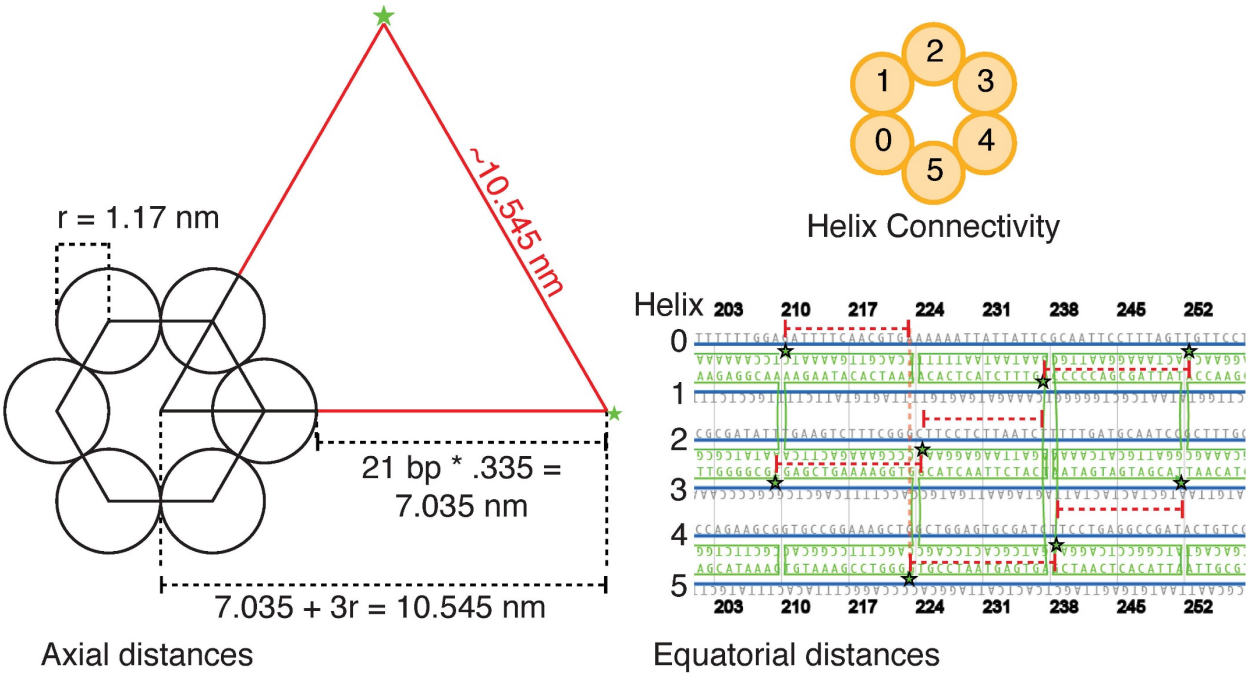

Helix A	Helix B	Axial D (nm)	Equatorial D (NT)	D/NT (nm)	Equatorial D (nm)	Total D (nm)
0	1	10.545	16	0.335	5.36	11.83
1	2	10.545	14	0.335	4.69	11.54
2	3	10.545	16	0.335	5.36	11.83
3	4	10.545	14	0.335	4.69	11.54
4	5	10.545	16	0.335	5.36	11.83
5	0	10.545	14	0.335	4.69	11.54

Figure S3. Distances between fluorophores.
21-bp handles extend from the 3' end of green staple strands (green stars). Distances between adjacent fluorophores were calculated as follows: sqrt((axial d)^2 + (equatorial d)^2). The radius of a double helix in a 6hb nanotube was measured previously (Gan et al., 2013).

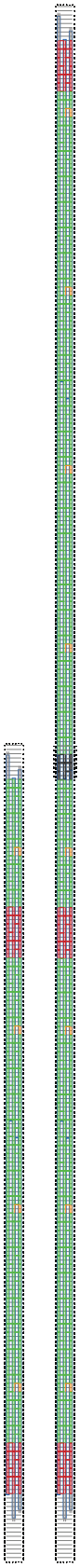

Figure S4. Design (caDNAno) diagrams of DNA-origami nanotubes
Staples in monomeric (left) and dimeric (right) structures are color-coded. All handles extend from 3' end.
Gray: poly-T end caps.
Red: Handles reserved for barcoding fluorophores. Handles are outer 2 or handle ix, depending on structure.
Green: optional attachment of inner 1 handle (for mEGFP/SiR).
Orange: non ATG 1 handle for biotin.
Black: linker DNA for dimerization.

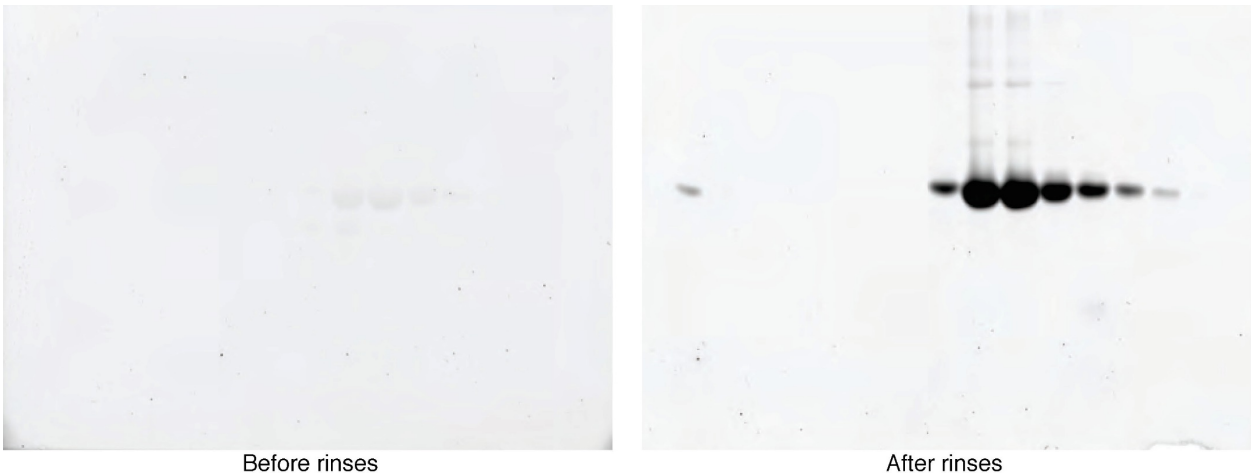

Figure S5. mEGFP in-gel fluorescence recovery.
After rinsing in water 3× 20 min, enough fluorescence was recovered to allow gel imaging in the 488 channel.

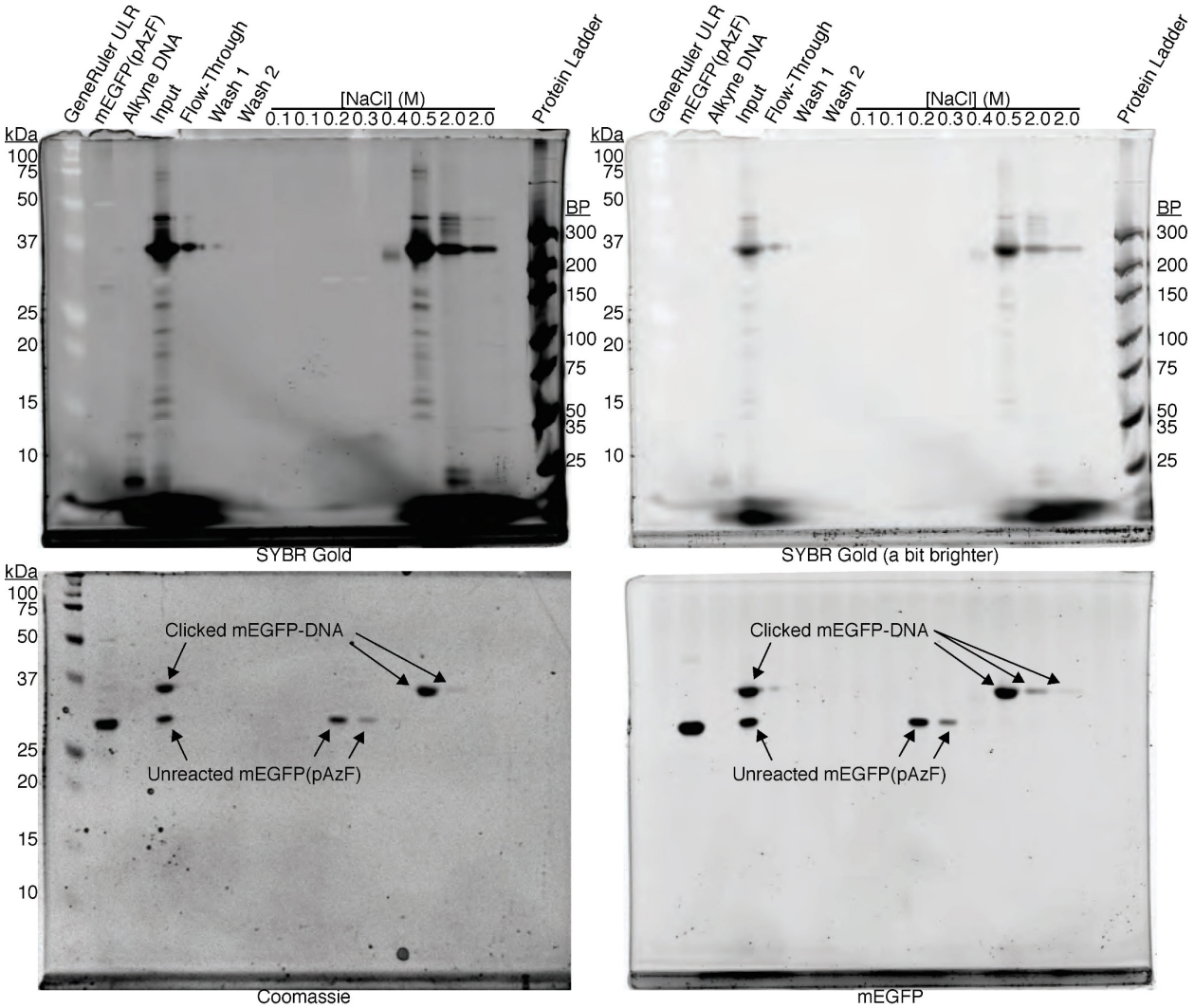

Figure S6. mEGFP-DNA conjugates after anion-exchange purification.
The expected ~7 kDa shift in reacted mEGFP:anti-inner1 is clearly visible when comparing unreacted mEGFP(pAzF) and the Input reaction mixture. Unreacted mEGFP(pAzF) began to elute at an ionic strength of 0.2 M NaCl, while mEGFP:anti-Inner1 eluted above 0.4 M NaCl. Incomplete reaction of mEGFP(pAzF) is possibly due to imperfect incorporation of pAzF at the C-term and azide reduction *in vivo* (Milles et al., 2012).

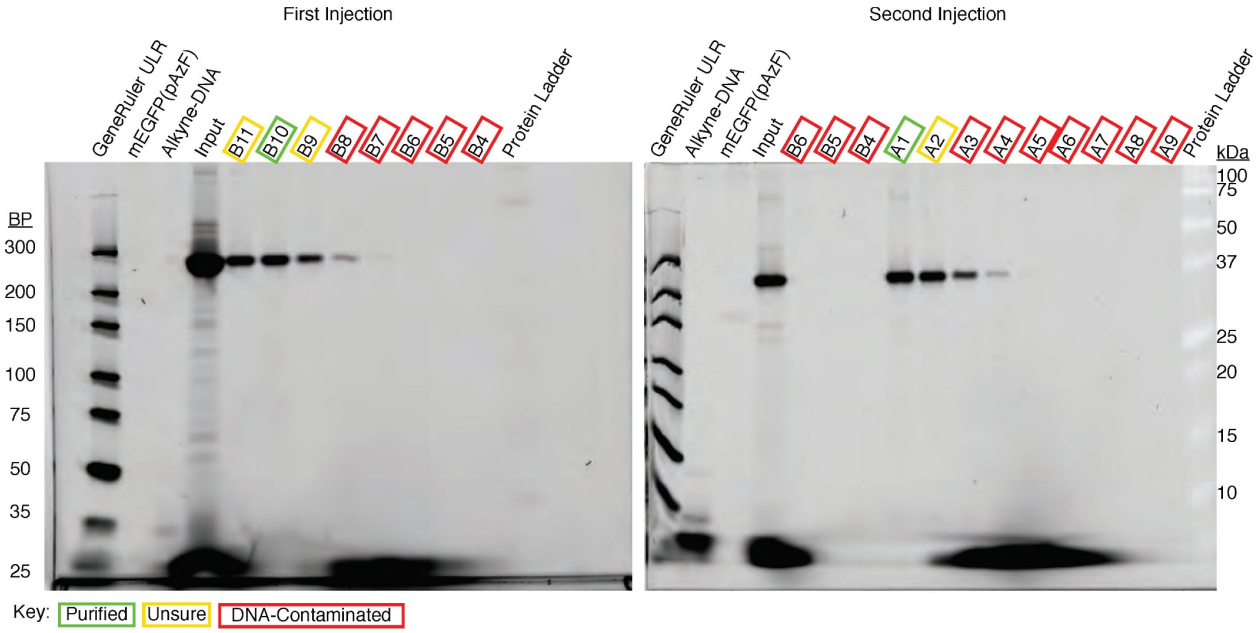

Figure S7. mEGFP-DNA conjugates after size-exclusion purification.
Anion-exchanged reaction mixtures were purified (two rounds) by size-exclusion chromatography to remove unreacted alkyne-DNA. Gels were stained by Sybr Gold and imaged in the corresponding channel.

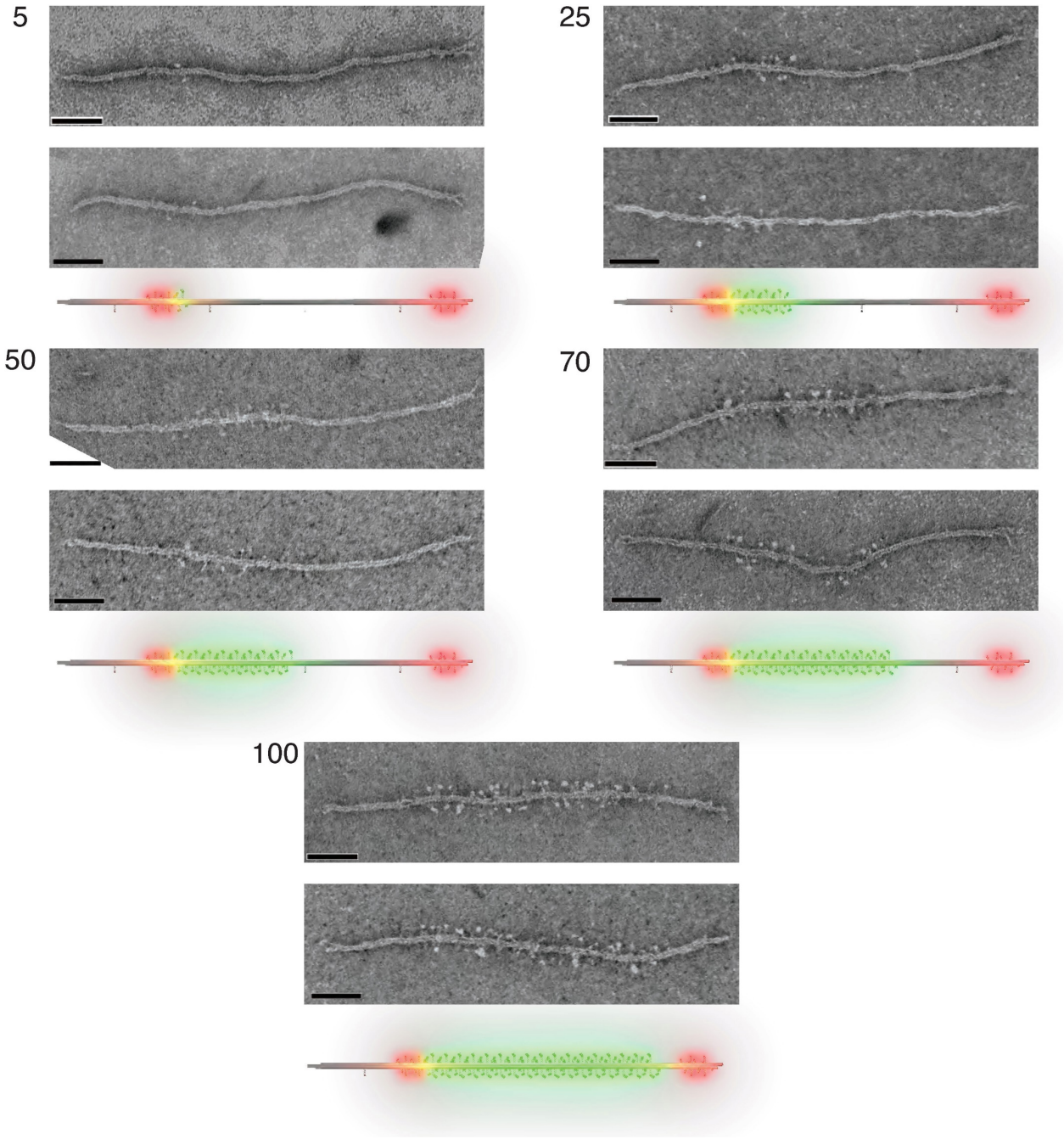

Figure S8. TEM micrographs of mEGFP standards.
5, 25, 50, 70, & 100 indicate the number of mEGFP each structure is designed to accommodate. All structures have 12 Alexa Fluor 647 at each end. Due to the resolution limit of negative-stain TEM, we do not expect to resolve every single mEGFP molecule. Nevertheless, in selected images, small dots (mEGFP) were found spanning the structures in the expected regions. Cartoon models were placed below micrographs (Green: GFP, Red: Alex Fluor 647) for direct comparison. Scale bars: 50 nm.

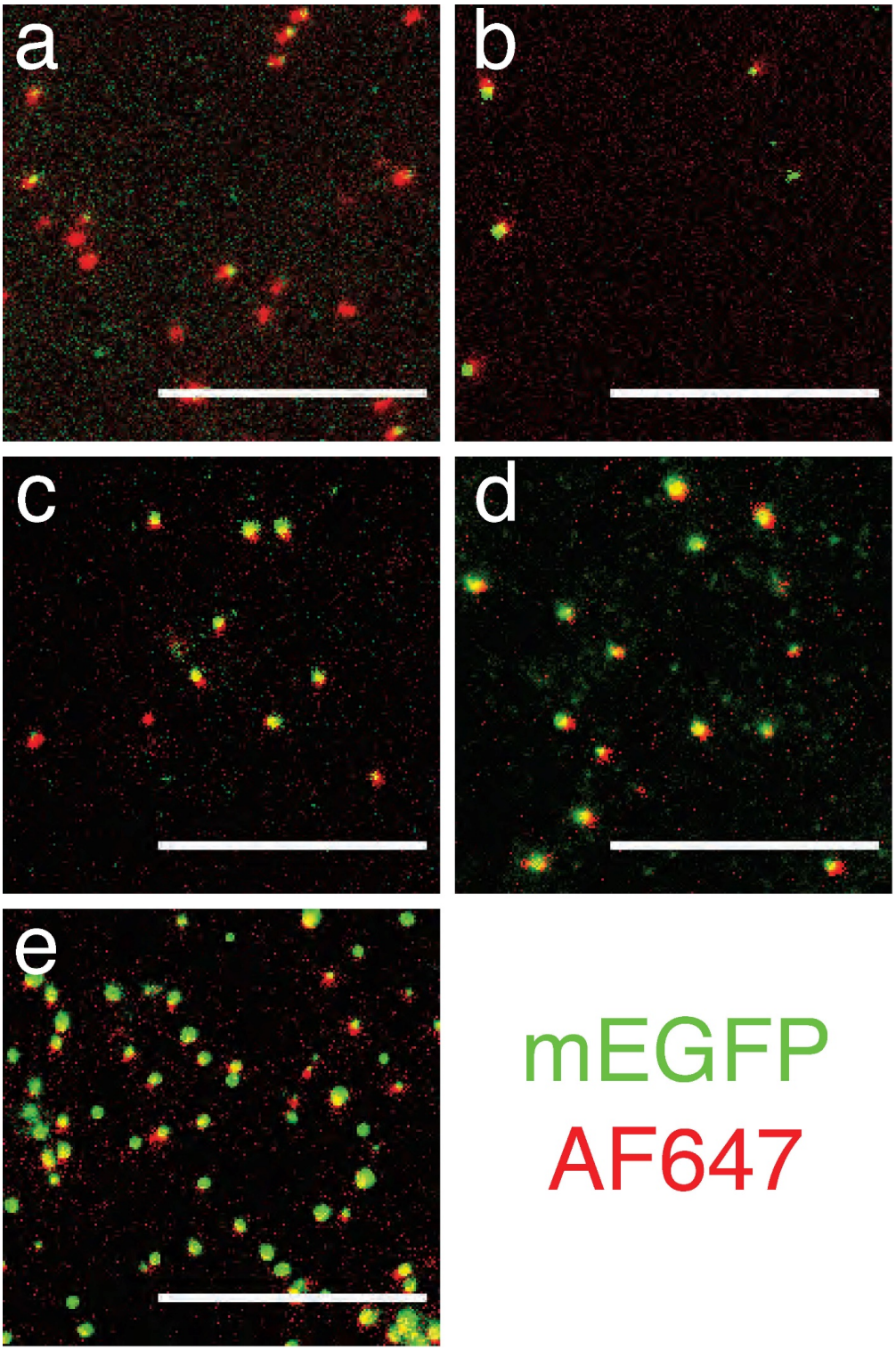

Figure S9. Wide-field fluorescence micrographs of mEGFP standards.
(a) 5×, (b) 25×, (c) 50×, (d) 70×, (e) 100×. All structures have 12 Alexa Fluor 647 at each end. Brightness and contrast for each image adjusted individually for clarity. Scale bars: 10 μm.

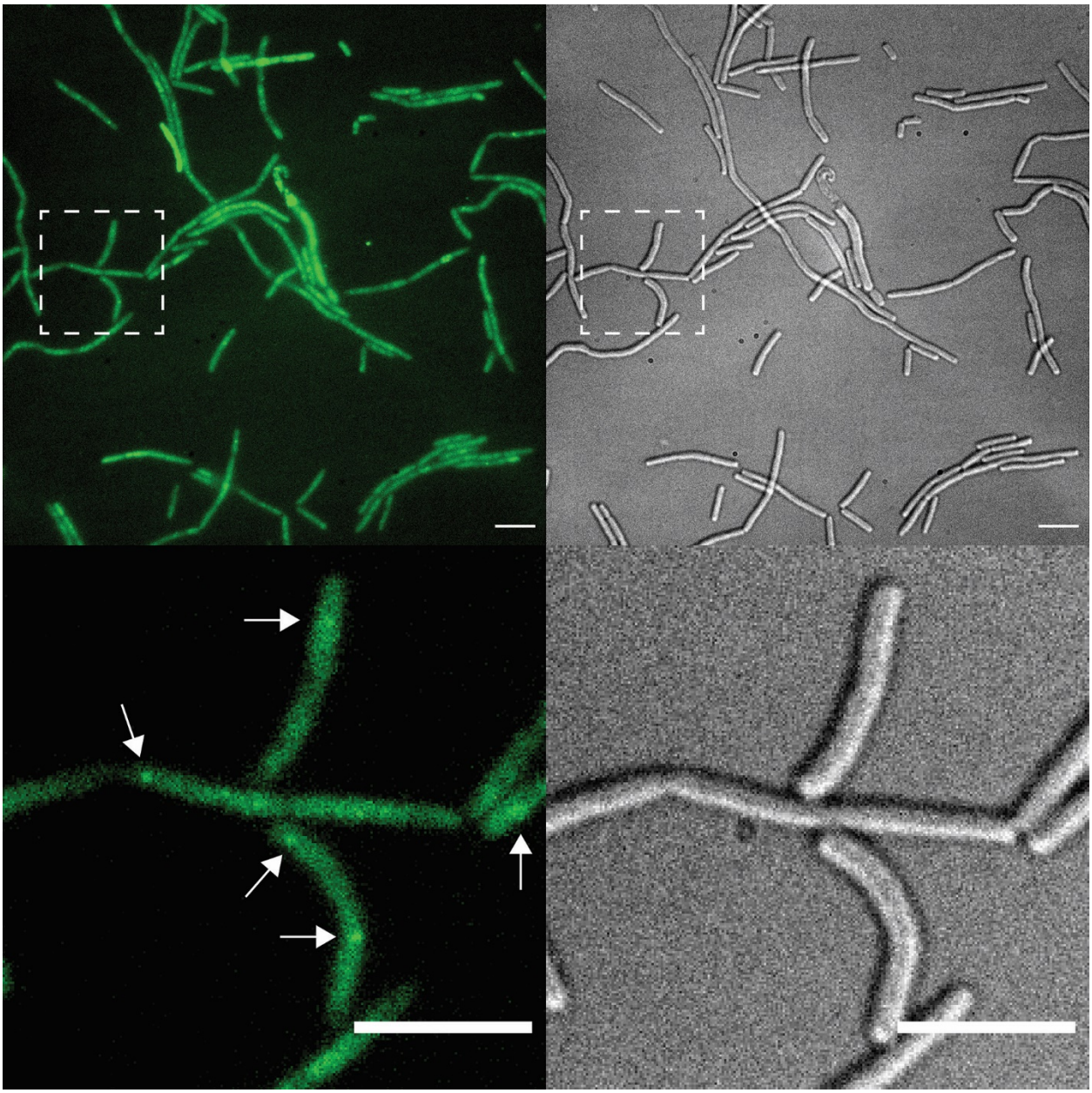

Figure S10. Wide-field fluorescence micrographs of B. subtilis.
Representative image of *B. subtilis* (strain NW001) cells expressing dnaC-mEGFP (puncta indicated by arrows). Left: mEGFP (488 nm); right: differential interference contrast. Images in the bottom row are magnified from areas within dotted rectangles. Brightness and contrast for each image adjusted individually for clarity. Unlike Figure 1d, the fluorescence brightness is rescaled not to highlight individual punctum, but to show the overall cell shapes. Scale bars: 10 μm.

Figure S11. SiR-DNA conjugate analyzed by PAGE.
SYBR Gold-stained 15% urea-PAGE gel of the SiR conjugate before (B) and after (A) purification. Ladder (L) is NEB Ultra Low Range DNA Ladder.

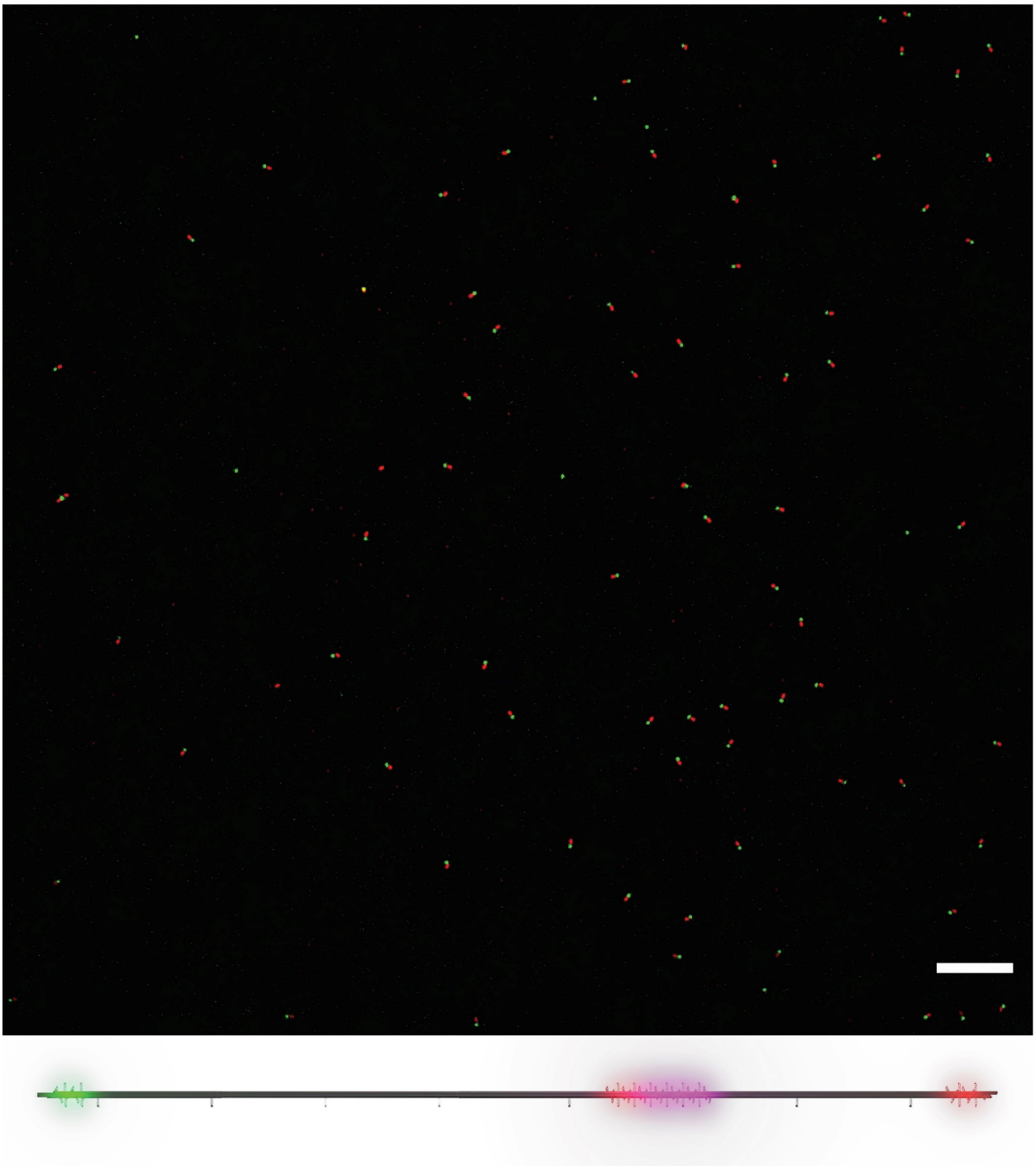

Figure S12. Fluorescent barcode pattern on 25× SiR standard.
Top: confocal fluorescence micrograph showing the barcoding channels of Alexa Fluor 488 (green), and TAMRA (red). Scale bar: 10 μm. Bottom: A 3D model showing positions of barcoding fluorophores on the 25×SiR-labeled DNA-origami 6hb structure.

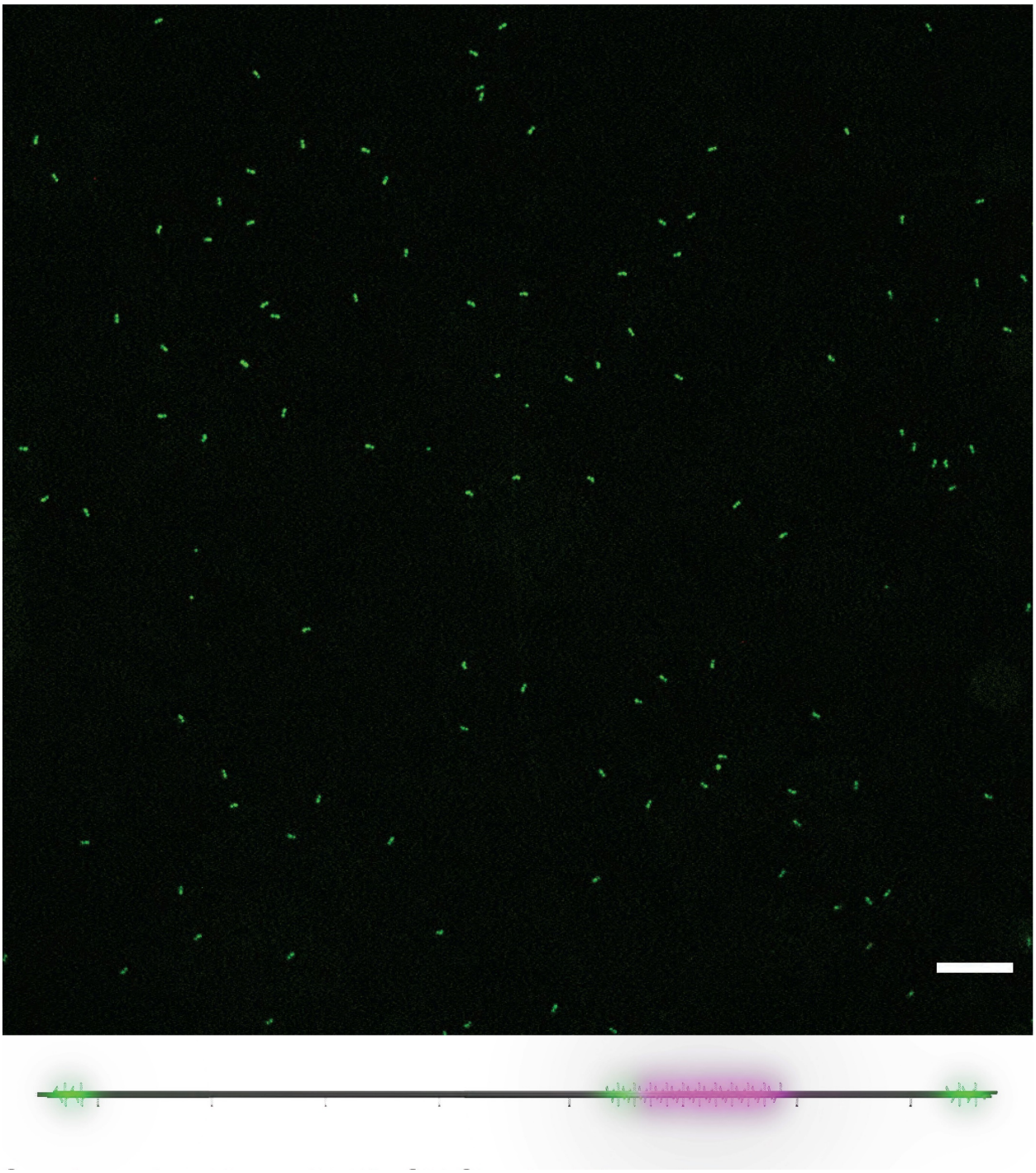

Figure S13. Fluorescent barcode pattern on 50× SiR standard.
Top: confocal fluorescence micrograph showing the barcoding channel of Alexa Fluor 488 (green). Scale bar: 10 μm. Bottom: A 3D model showing positions of barcoding fluorophores on the 50×SiR-labeled DNA-origami 6hb structure.

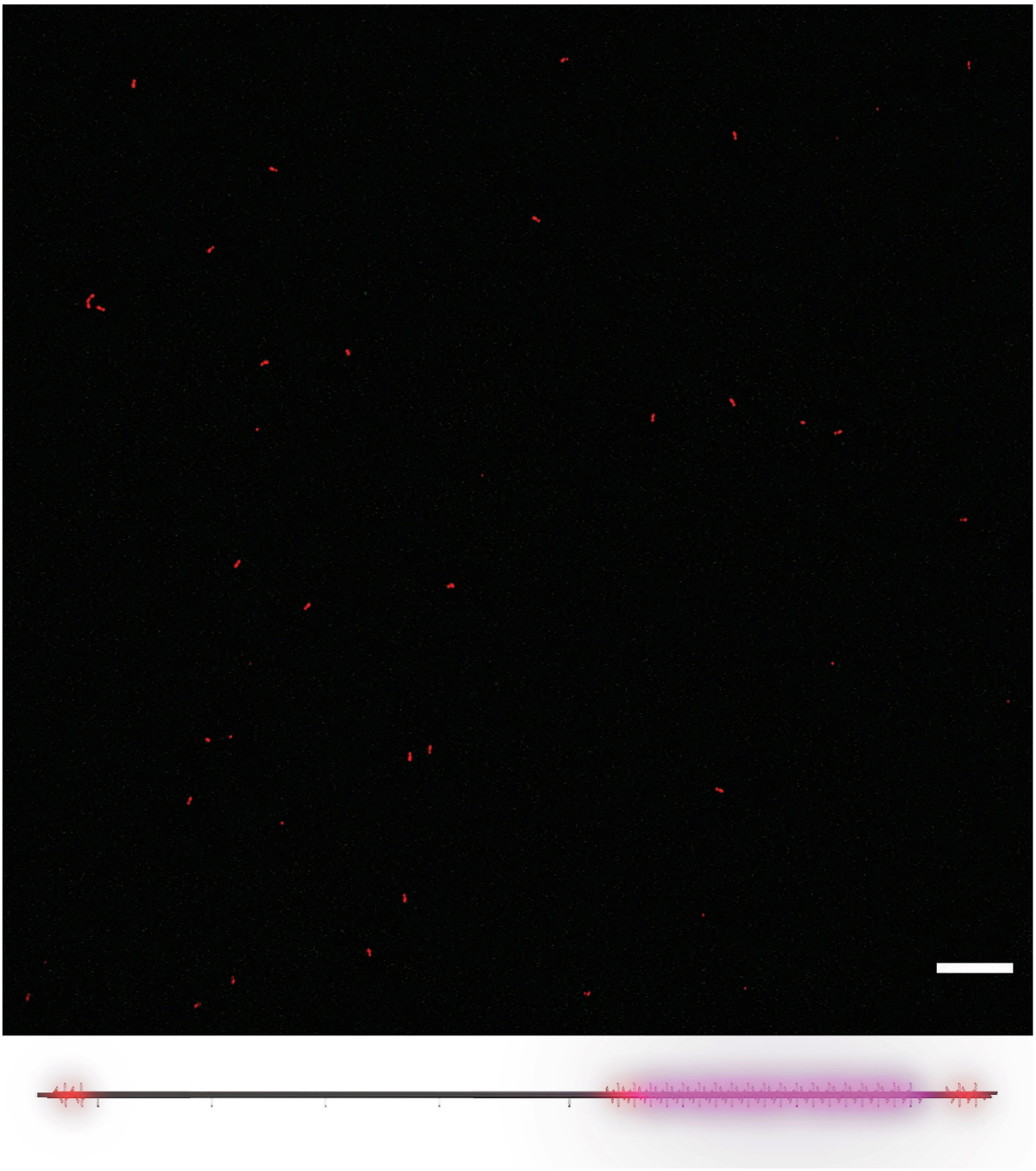

Figure S14. Fluorescent barcode pattern on 100× SiR standard.
Top: confocal fluorescence micrograph showing the barcoding channel of TAMRA (red). Scale bar: 10 μm. Bottom: A 3D model showing positions of barcoding fluorophores on the 100×SiR-labeled DNA-origami 6hb structure.

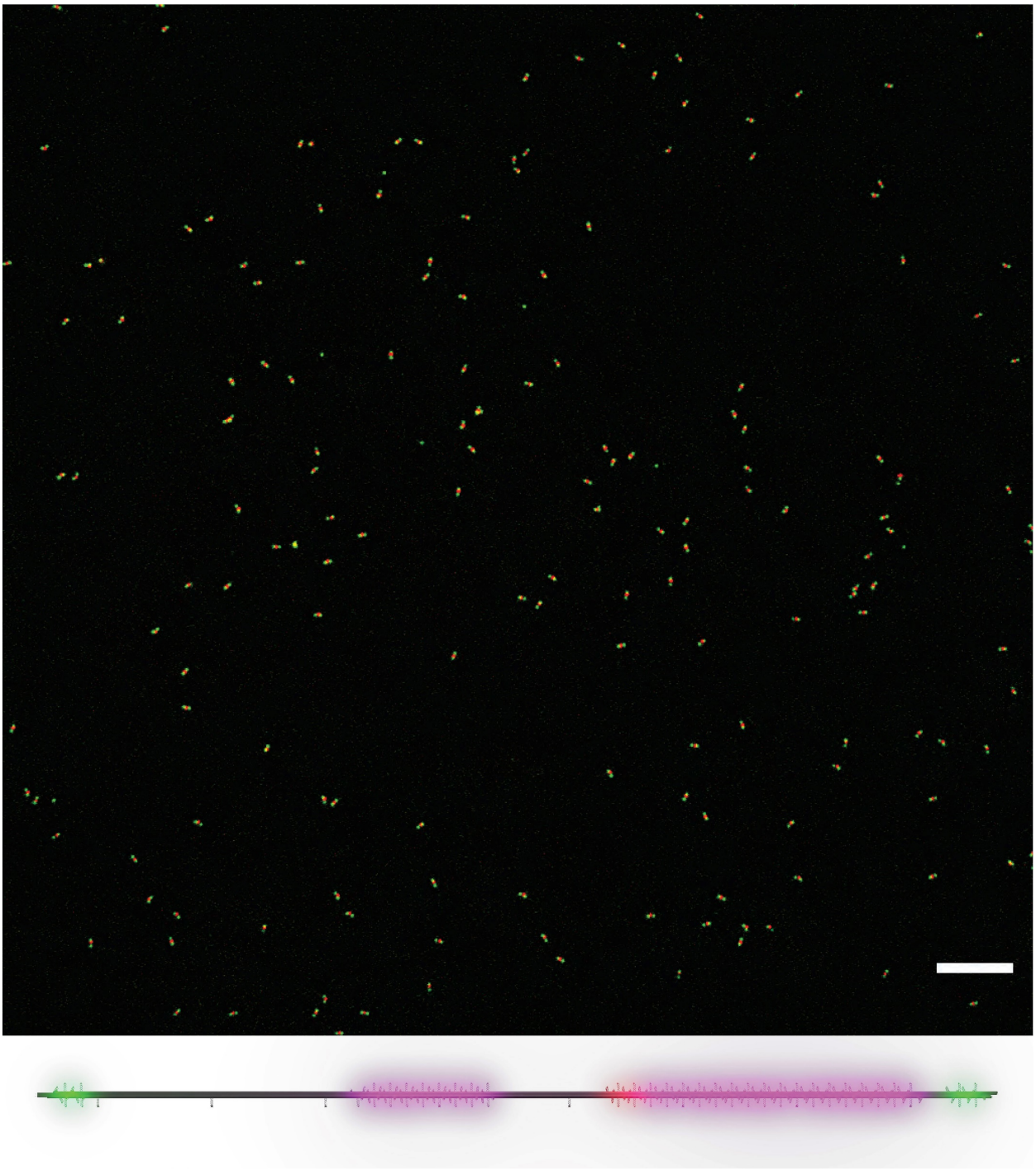

Figure S15. Fluorescent barcode pattern on 150× SiR standard.
Top: confocal fluorescence micrograph showing the barcoding channels of Alexa Fluor 488 (green), and TAMRA (red). Scale bar: 10 μm. Bottom: A 3D model showing positions of barcoding fluorophores on the 150×SiR-labeled DNA-origami 6hb structure.

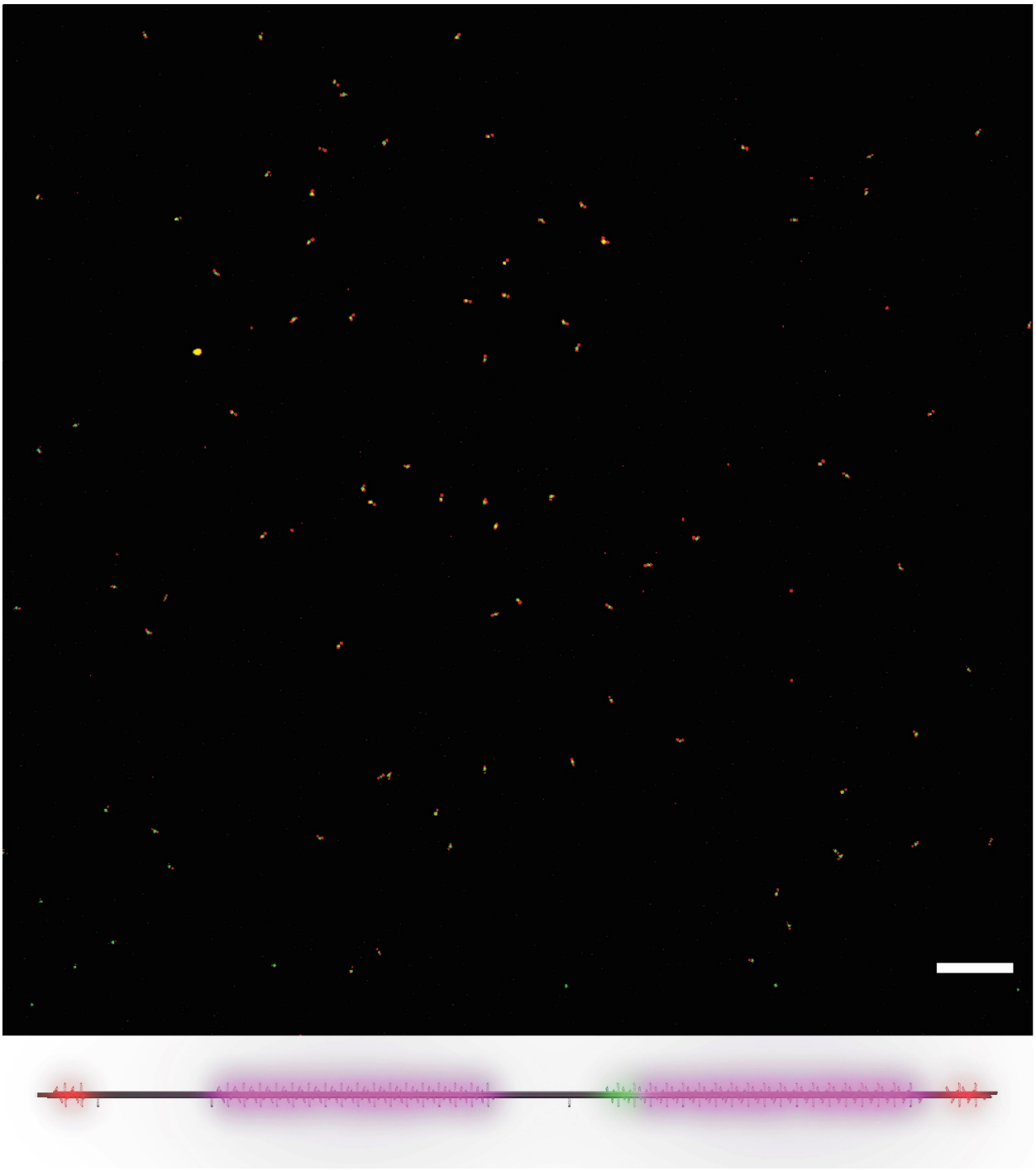

Figure S16. Fluorescent barcode pattern on 200× SiR standard.
Top: confocal fluorescence micrograph showing the barcoding channels of Alexa Fluor 488 (green), and TAMRA (red). Scale bar: 10 μm. Bottom: A 3D model showing positions of barcoding fluorophores on the 200×SiR-labeled DNA-origami 6hb structure.

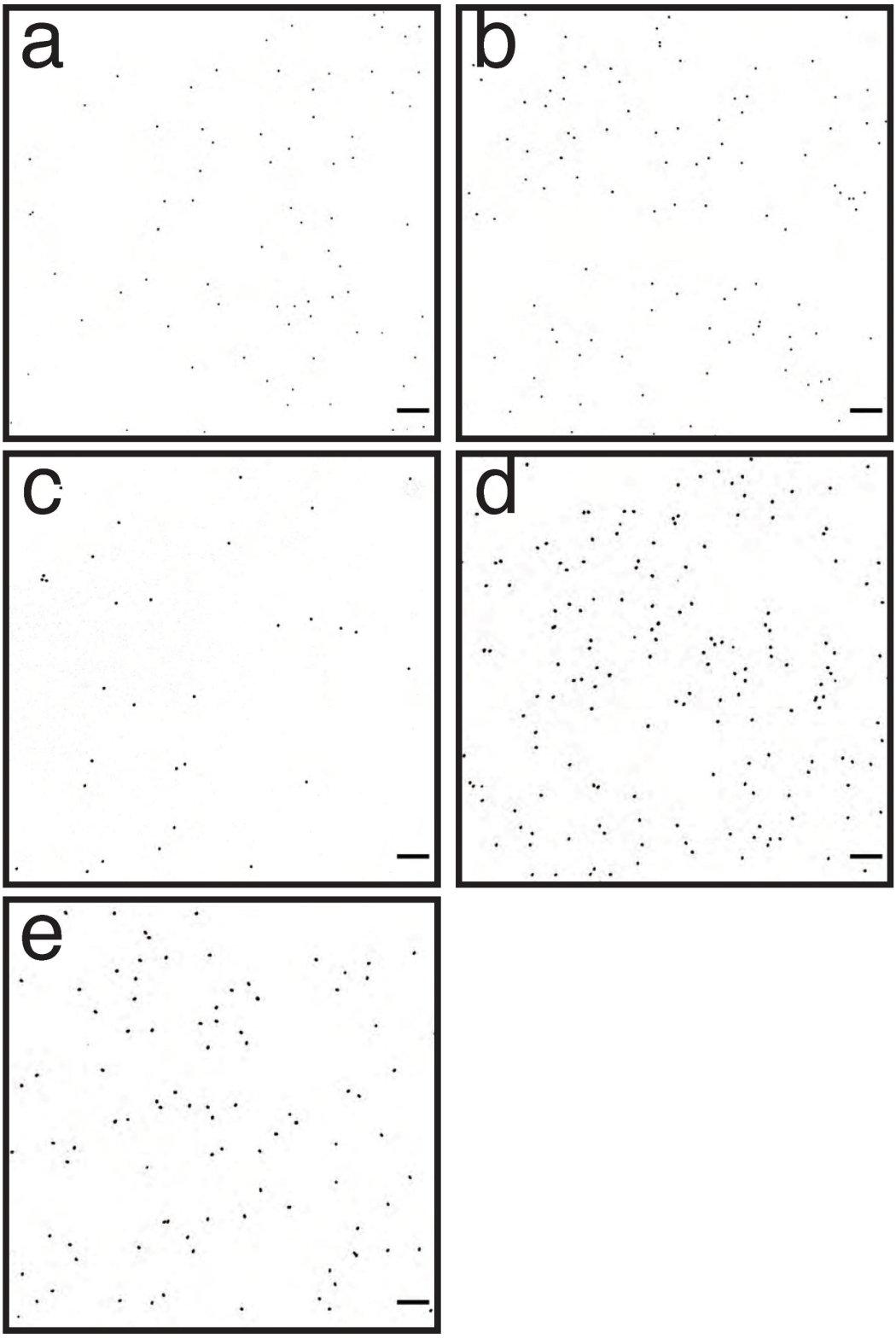

Figure S17. Confocal fluorescence micrographs of SiR standards.
Panels show the SiR channel of Figure S17–S21, respectively: (a) 25× SiR, (b) 50× SiR, (c) 100× SiR, (d) 150× SiR, (e) 200× SiR. All panels are adjusted to the same brightness and contrast levels, and color-inverted for visual clarity. Scale bars: 10 μm.

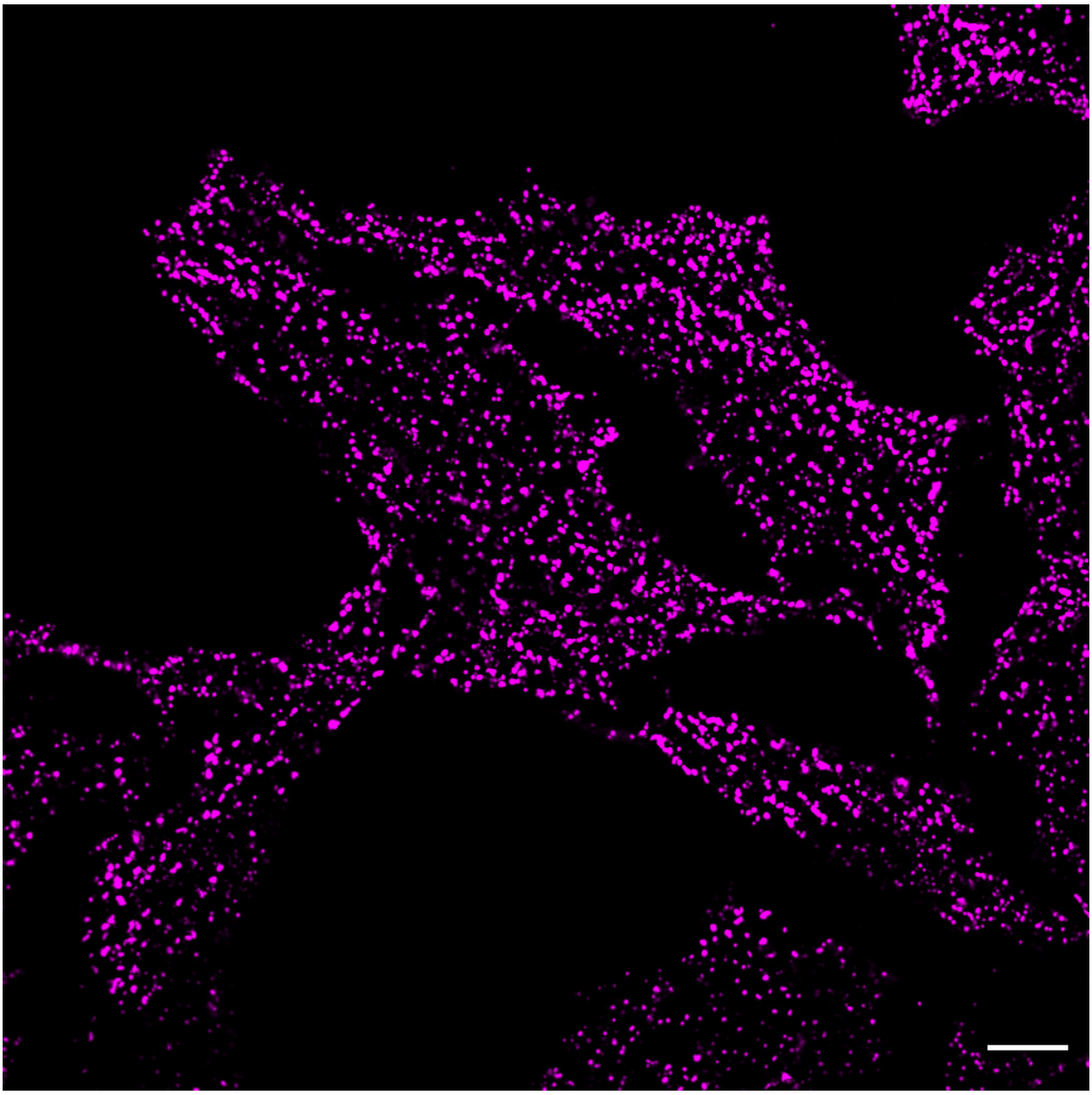

Figure S18. A confocal fluorescence micrograph of Hela cells.
The focal plane is set close to the bottom of the dish. Scale bar: 10 μm.

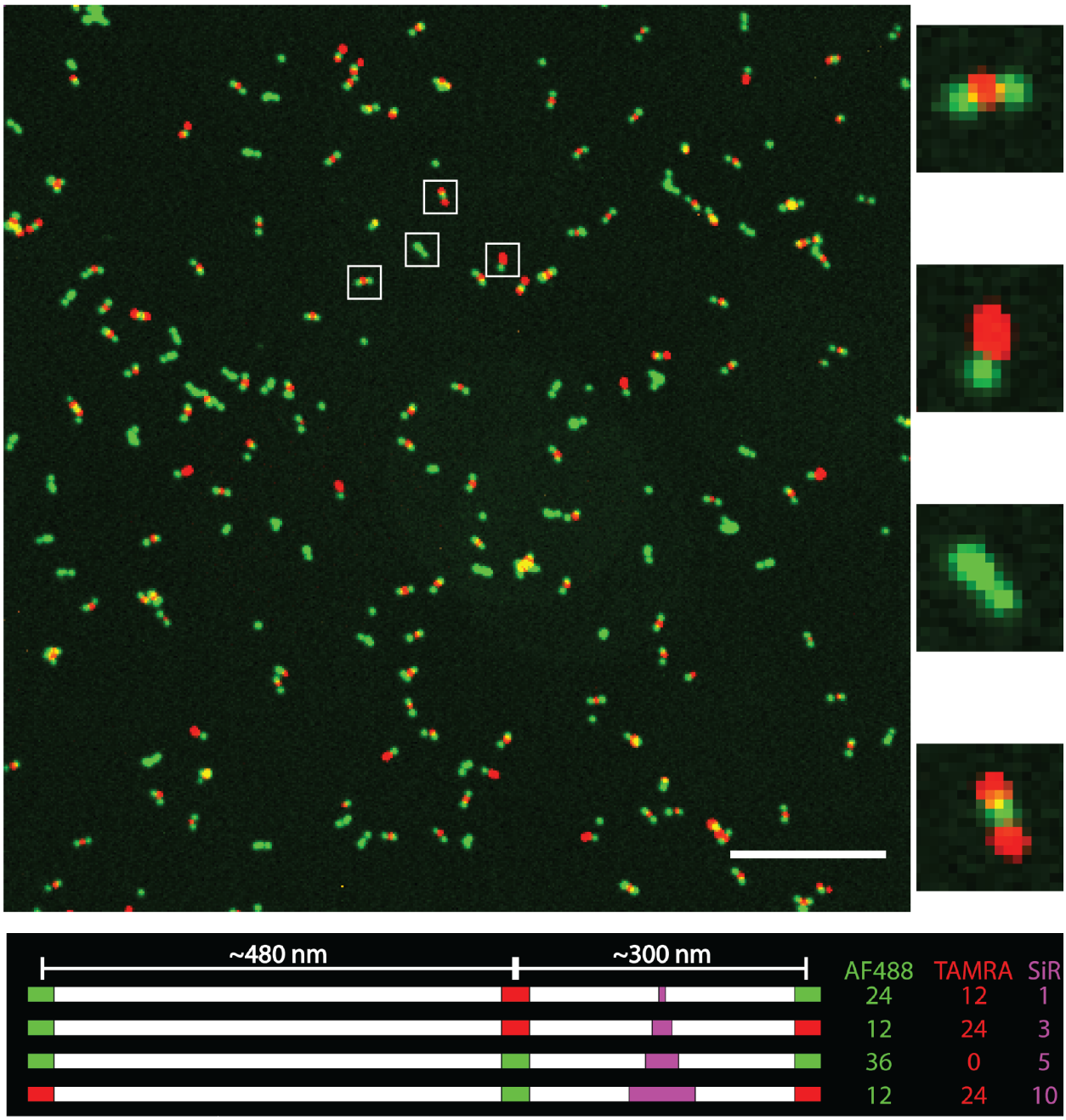

Figure S19. Multiple DNA-origami barcodes imaged together.

Different DNA-origami 6hb structures (designed to display 1–10 SiR molecules) with distinct barcodes were mixed and imaged in 1× TE + 10 mM MgCl2 using a TIRF microscope. DNA structures were fixed on a glass coverslip via biotin-streptavidin binding. Each imaging standard species is readily distinguishable from the image, which could enable multiplexed imaging. Pseudo-colors: Alexa Fluor 488 (green) and TAMRA (red). Scale bar: 10 μm.

Table S1. Handle and antihandle sequences

Name	**Sequence (5'-3')**
Outer 2	**CTTCACACCACACTCCATCTA**
Inner 1	**AAATTATCTACCACAACTCAC**
handle ix	**ACCTACTAACATAATCATCAC**
Non ATG 1 handle	**CGGTTGTACTGTGACCGATTC**
Anti Outer 2	**TAGATGGAGTGTGGTGTGAAG**
Anti Inner 1	**GTGAGTTGTGGTAGATAATTT**
anti-handle ix	**GTGATGATTATGTTAGTAGGT**
Non-ATG 1 antihandle	**GAATCGGTCACAGTACAACCG**
5'Alkyne-anti Inner 1	**/5Hexynyl/GTGAGTTGTGGTAGATAATTT**
5' Biotin Non-ATG 1	**/5Biosg/GAATCGGTCACAGTACAACCG**
3'AF488-anti Inner 1	**GTGAGTTGTGGTAGATAATTT/3AlexF488N/**
5' AF488-anti handle ix	**/5Alex488N/TGTGATGATTATGTTAGTAGGT**
5' TAMRA-anti handle ix	**/56-TAMN/GTGATGATTATGTTAGTAGGT**
5' TAMRA-anti outer 2	**/56-TAMN/TAGATGGAGTGTGGTGTGAAG**
5' AF647-anti outer 2	**/5Alex647N/TAGATGGAGTGTGGTGTGAAG**

Table S2. Linker DNA strands used in dimers

Name	**Sequence (5'-3')**
LD1.1	CATTGCATGCCTGCGGAATTAGAGCCAGAAAGGTGAATTATC
LD1.2	CCAGTGCCAAGCGATTTGAAATACCGACAGAAAAAGCCTGTT
LD1.3	ACCGTCACCGACCCGAATCATAATTACTCGTGTGATAAATAA
LD1.4	GGTTGAGCCATTTGAGGTCGACTCTAGATTGTAAAACGACGG
LD1.5	GGCGTTAAATAACATCCCAGTCACGACGCCTTTGATAGCGAG
LD1.6	AAGAATAAACACCGGCTTTTGCGGGATCTGCAGGGAGTTAAA

Table S3. Linker DNA strands used in dimers

	mEGFP-labeled samples		SiR-labeled samples		
Microscope	Leica DMi8 wide-field inverted microscope		Nikon TiE inverted confocal with Yokogawa CSU-W1 spinning disk (50 um disk pattern)		
Light source	Lumencor spectraX (LED)		Multiple lasers		
Objective	HC Plan Apochromat 100×DIC, WD 90 μm, No: 11506381		CFI Plan Apochromat Lambda 60x/1.4 Oil, WD 0.13 mm, No: MRD01605		
Camera	Andor iXon Ultra888 EMCCD		Andor iXon Ultra888 EMCCD		
Fluorophore	mEGFP	AF647	SiR	AF488	TAMRA
Excitation wavelength (nm)	470/24-25	640/30-25	647	488	561
Excitation filter (nm)	470/40	620/60	N.A.	N.A.	N.A.
Dichroic mirror (nm)	495	660	405/488/561/647		
Emission filter (nm)	500-550	700/75	700/75	525/36	605/70
Excitation power	50%	10%	190 mW*, 70%	130 mW*, 40%	130 mW*, 40%
Exposure time (s)	1	1	1	1	1

*Laser power measured at fiber tip.

References

Acuna, G. P., Möller, F. M., Holzmeister, P., Beater, S., Lalkens, B., & Tinnefeld, P. (2012). Fluorescence Enhancement at Docking Sites of DNA-Directed Self-Assembled Nanoantennas. *Science (New York, N.Y.)*, *338*(6), 506. https://doi.org/10.1126/science.1228638

Akamatsu, M., Lin, Y., Bewersdorf, J., & Pollard, T. D. (2017). Analysis of interphase node proteins in fission yeast by quantitative and superresolution fluorescence microscopy. *Molecular Biology of the Cell*, *28*(23), 3203–3214. https://doi.org/10.1091/mbc.e16-07-0522

Amiram, M., Haimovich, A. D., Fan, C., Wang, Y.-S., Aerni, H.-R., Ntai, I., Moonan, D. W., Ma, N. J., Rovner, A. J., Hong, S. H., Kelleher, N. L., Goodman, A. L., Jewett, M. C., Söll, D., Rinehart, J., & Isaacs, F. J. (2015). Evolution of translation machinery in recoded bacteria enables multi-site incorporation of nonstandard amino acids. *Nature Biotechnology*, *33*(12), 1272–1279. https://doi.org/10.1038/nbt.3372

Auer, A., Schlichthaerle, T., Woehrstein, J. B., Schueder, F., Strauss, M. T., Grabmayr, H., & Jungmann, R. (2018). Nanometer-scale Multiplexed Super-Resolution Imaging with an Economic 3D-DNA-PAINT Microscope. *ChemPhysChem*, *19*(22), 3024–3034. https://doi.org/10.1002/cphc.201800630

Bacia, K., & Schwille, P. (2003). A dynamic view of cellular processes by in vivo fluorescence auto- and cross-correlation spectroscopy. *Methods (San Diego, Calif.)*, *29*(1), 74–85. https://doi.org/10.1016/s1046-2023(02)00291-8

Bailey, S., Eliason, W. K., & Steitz, T. A. (2007). The crystal structure of the Thermus aquaticus DnaB helicase monomer. *Nucleic Acids Research*, *35*(14), 4728–4736. https://doi.org/10.1093/nar/gkm507

Beilen, J. W. A. van, & Brul, S. (2013). Compartment-specific pH monitoring in Bacillus subtilis using fluorescent sensor proteins: a tool to analyze the antibacterial effect of weak organic acids. *Frontiers in Microbiology*, *4*. https://doi.org/10.3389/fmicb.2013.00157

Bellot, G., McClintock, M. A., Chou, J. J., & Shih, W. M. (2013). DNA nanotubes for NMR structure determination of membrane proteins. *Nature Protocols*, *8*(4), 755–770. https://doi.org/10.1038/nprot.2013.037

Berro, J., & Pollard, T. D. (2014). Synergies between Aip1p and capping protein subunits (Acp1p and Acp2p) in clathrin-mediated endocytosis and cell polarization in fission yeast. *Molecular Biology of the Cell*, *25*(22), 3515–3527. https://doi.org/10.1091/mbc.e13-01-0005

Bulseco, D. A., & Wolf, D. E. (2013). *Fluorescence Correlation Spectroscopy: Molecular Complexing in Solution and in Living Cells* (4th ed., Vol. 114). Elsevier Inc. https://doi.org/10.1016/b978-0-12-407761-4.00021-x

Castro, C. E., Kilchherr, F., Kim, D.-N., Shiao, E. L., Wauer, T., Wortmann, P., Bathe, M., & Dietz, H. (2011). A primer to scaffolded DNA origami. *Nature Methods*, *8*(3), 221–229. https://doi.org/10.1038/nmeth.1570

Cheng, Y., Boll, W., Kirchhausen, T., Harrison, S. C., & Walz, T. (2007). Cryo-electron Tomography of Clathrin-coated Vesicles: Structural Implications for Coat Assembly. *Journal of Molecular Biology*, *365*(3), 892–899. https://doi.org/10.1016/j.jmb.2006.10.036

Chung, K. K., Zhang, Z., Kidd, P., Zhang, Y., Williams, N. D., Rollins, B., Yang, Y., Lin, C., Baddeley, D., & Bewersdorf, J. (2020). Fluorogenic probe for fast 3D whole-cell DNA-PAINT. *BioRxiv*, 2020.04.29.066886. https://doi.org/10.1101/2020.04.29.066886

Coffman, V C, & Wu, J. Q. (2014). Every laboratory with a fluorescence microscope should consider counting molecules. *Molecular Biology of the Cell*, *25*(10), 1545–1548. https://doi.org/10.1091/mbc.e13-05-0249

Coffman, V., Lee, I.-J., & Wu, J.-Q. (2014). *Counting Molecules Within Cells*. Biota Publishing.

Coffman, Valerie C, & Wu, J.-Q. (2012). Counting protein molecules using quantitative fluorescence microscopy. *Trends in Biochemical Sciences*, *37*(11), 499–506. https://doi.org/10.1016/j.tibs.2012.08.002

Cong, L., Ran, F. A., Cox, D., Lin, S., Barretto, R., Habib, N., Hsu, P. D., Wu, X., Jiang, W., Marraffini, L. A., & Zhang, F. (2013). Multiplex genome engineering using

CRISPR/Cas systems. *Science (New York, N.Y.)*, *339*(6121), 819–823. https://doi.org/10.1126/science.1231143

Czogalla, A., Petrov, E. P., Kauert, D. J., Uzunova, V., Zhang, Y., Seidel, R., & Schwille, P. (2013). Switchable domain partitioning and diffusion of DNA origami rods on membranes. *Faraday Discuss.*, *161*, 31–43. https://doi.org/10.1039/c2fd20109g

Dietz, H., Douglas, S. M., & Shih, W. M. (2009). Folding DNA into twisted and curved nanoscale shapes. *Science (New York, N.Y.)*, *325*(5941), 725–730. https://doi.org/10.1126/science.1174251

Ditlev, J. A., Michalski, P. J., Huber, G., Rivera, G. M., Mohler, W. A., Loew, L. M., & Mayer, B. J. (2012). Stoichiometry of Nck-dependent actin polymerization in living cells. *The Journal of Cell Biology*, *197*(5), 643–658. https://doi.org/10.1083/jcb.201111113

Douglas, S. M., Bachelet, I., & Church, G. M. (2012). A logic-gated nanorobot for targeted transport of molecular payloads. *Science (New York, N.Y.)*, *335*(6070), 831–834. https://doi.org/10.1126/science.1214081

Douglas, S. M., Chou, J. J., & Shih, W. M. (2007). DNA-nanotube-induced alignment of membrane proteins for NMR structure determination. *Proceedings of the National Academy of Sciences of the United States of America*, *104*(16), 6644–6648. https://doi.org/10.1073/pnas.0700930104

Douglas, S. M., Dietz, H., Liedl, T., Högberg, B., Graf, F., & Shih, W. M. (2009). Self-assembly of DNA into nanoscale three-dimensional shapes. *Nature*, *459*(7245), 414–418. https://doi.org/10.1038/nature08016

Douglas, S. M., Marblestone, A. H., Teerapittayanon, S., Vazquez, A., Church, G. M., & Shih, W. M. (2009). Rapid prototyping of 3D DNA-origami shapes with caDNAno. *Nucleic Acids Research*, *37*(15), 5001–5006. https://doi.org/10.1093/nar/gkp436

Ducret, A., Quardokus, E. M., & Brun, Y. V. (2016). *MicrobeJ, a tool for high throughput bacterial cell detection and quantitative analysis*. 1–7. https://doi.org/10.1038/nmicrobiol.2016.77

Ehrlich, M., Boll, W., Oijen, A. van, Hariharan, R., Chandran, K., Nibert, M. L., & Kirchhausen, T. (2004). Endocytosis by Random Initiation and Stabilization of Clathrin-Coated Pits. *Cell*, *118*(5), 591–605. https://doi.org/10.1016/j.cell.2004.08.017

El-Sagheer, A. H., & Brown, T. (2010). Click chemistry with DNA. *Chemical Society Reviews*, *39*(4), 1388–19. https://doi.org/10.1039/b901971p

Escher, M. (1955). *Depth* [Wood engraving and woodcut in colors].

Fan, S., Wang, D., Kenaan, A., Cheng, J., Cui, D., & Song, J. (2019). Create Nanoscale Patterns with DNA Origami. *Small*, *15*(26), e1805554. https://doi.org/10.1002/smll.201805554

Fass, D., Bogden, C. E., & Berger, J. M. (1999). Crystal structure of the N-terminal domain of the DnaB hexameric helicase. *Structure*, *7*(6), 691–698. https://doi.org/10.1016/s0969-2126(99)80090-2

Fu, T. J., & Seeman, N. C. (1993). DNA double-crossover molecules. *Biochemistry*, *32*(13), 3211–3220. https://doi.org/10.1021/bi00064a003

Gan, L., Chao, T.-C., Camacho-Alanis, F., & Ros, A. (2013). Six-helix bundle and triangle DNA origami insulator-based dielectrophoresis. *Analytical Chemistry*, *85*(23), 11427–11434. https://doi.org/10.1021/ac402493u

Gao, Q., Courtheoux, T., Gachet, Y., Tournier, S., He, X., & McIntosh, J. R. (2010). A non-ring-like form of the Dam1 complex modulates microtubule dynamics in fission yeast. *Proceedings of the National Academy of Sciences of the United States of America*, *107*(30), 13330–13335. https://doi.org/10.2307/25708716?ref=no-x-route:bb23eefb277f3599508628c4e58233fc

GraphPad Prism (8.4.3). (2020). [MacOS]. GraphPad Software.

Gruβmayer, K. S., Yserentant, K., & Herten, D.-P. (2019). Photons in - numbers out: perspectives in quantitative fluorescence microscopy for in situprotein counting. *Methods and Applications in Fluorescence*, *7*(1), 012003–012021. https://doi.org/10.1088/2050-6120/aaf2eb

Harris, J. R., & Marles-Wright, J. (2017). *Macromolecular Protein Complexes*. Springer.

Haustein, E., & Schwille, P. (2007). Fluorescence correlation spectroscopy: novel variations of an established technique. *Annu Rev Biophys Biomol Struct*, *36*, 151–169. https://doi.org/10.1146/annurev.biophys.36.040306.132612

Hoelz, A., Debler, E. W., & Blobel, G. (2011). The structure of the nuclear pore complex. *Annual Review of Biochemistry*, *80*, 613–643. https://doi.org/10.1146/annurev-biochem-060109-151030

Ijäs, H., Nummelin, S., Shen, B., Kostiainen, M. A., & Linko, V. (2018). Dynamic DNA Origami Devices: from Strand-Displacement Reactions to External-Stimuli Responsive Systems. *International Journal of Molecular Sciences*, *19*(7). https://doi.org/10.3390/ijms19072114

Joglekar, A. P., Bouck, D. C., Molk, J. N., Bloom, K. S., & Salmon, E. D. (2006). Molecular architecture of a kinetochore–microtubule attachment site. *Nature Cell Biology*, *8*(6), 581–585. https://doi.org/10.1038/ncb1414

Joglekar, A. P., Salmon, E. D., & Bloom, K. S. (2008). Counting kinetochore protein numbers in budding yeast using genetically encoded fluorescent proteins. *Fluorescent Proteins, Second Edition*, *85*, 127-+. https://doi.org/10.1016/s0091-679x(08)85007-8

Jungmann, R., Avendaño, M. S., Dai, M., Woehrstein, J. B., Agasti, S. S., Feiger, Z., Rodal, A., & Yin, P. (2016). Quantitative super-resolution imaging with qPAINT. *Nature Methods*, *13*(5), 439–442. https://doi.org/10.1038/nmeth.3804

Jungmann, R., Avendaño, M. S., Woehrstein, J. B., Dai, M., Shih, W. M., & Yin, P. (2014). Multiplexed 3D cellular super-resolution imaging with DNA-PAINT and Exchange-PAINT. *Nature Methods*, *11*(3), 313–318. https://doi.org/10.1038/nmeth.2835

Jungmann, R., Steinhauer, C., Scheible, M., Kuzyk, A., Tinnefeld, P., & Simmel, F. C. (2010). Single-Molecule Kinetics and Super-Resolution Microscopy by Fluorescence Imaging of Transient Binding on DNA Origami. *Nano Letters*, *10*(11), 4756–4761. https://doi.org/10.1021/nl103427w

Jusuk, I., Vietz, C., Raab, M., Dammeyer, T., & Tinnefeld, P. (2015). Super-Resolution Imaging Conditions for enhanced Yellow Fluorescent Protein (eYFP) Demonstrated on DNA Origami Nanorulers. *Scientific Reports*, 1–9. https://doi.org/10.1038/srep14075

Kaplan, D. L., Saleh, O. A., & Ribeck, N. (2013). Single-molecule and bulk approaches to the DnaB replication fork helicase. *Frontiers in Bioscience-Landmark*, *18*(1), 224–240. https://doi.org/10.2741/4097

Khater, I. M., Nabi, I. R., & Hamarneh, G. (2020). A Review of Super-Resolution Single-Molecule Localization Microscopy Cluster Analysis and Quantification Methods. *Patterns*, *1*(3), 100038. https://doi.org/10.1016/j.patter.2020.100038

Kielar, C., Xin, Y., Shen, B., Kostiainen, M. A., Grundmeier, G., Linko, V., & Keller, A. (2018). On the Stability of DNA Origami Nanostructures in Low-Magnesium Buffers.

Angewandte Chemie International Edition, *57*(30), 9470–9474. https://doi.org/10.1002/anie.201802890

Kim, D.-N., Kilchherr, F., Dietz, H., & Bathe, M. (2012). Quantitative prediction of 3D solution shape and flexibility of nucleic acid nanostructures. *Nucleic Acids Research*, *40*(7), 2862–2868. https://doi.org/10.1093/nar/gkr1173

Kim, S. A., Heinze, K. G., & Schwille, P. (2007). Fluorescence correlation spectroscopy in living cells. *Nature Methods*, *4*(11), 963–973. https://doi.org/10.1038/nmeth1104

Kirchhausen, T., Owen, D., & Harrison, S. C. (2014). Molecular Structure, Function, and Dynamics of Clathrin-Mediated Membrane Traffic. *Cold Spring Harbor Perspectives in Biology*, *6*(5), a016725–a016725. https://doi.org/10.1101/cshperspect.a016725

Kopperger, E., List, J., Madhira, S., Rothfischer, F., Lamb, D. C., & Simmel, F. C. (2018). A self-assembled nanoscale robotic arm controlled by electric fields. *Science (New York, N.Y.)*, *359*(6373), 296–301. https://doi.org/10.1126/science.aao4284

Kurz, A., Schmied, J. J., Grußmayer, K. S., Holzmeister, P., Tinnefeld, P., & Herten, D.-P. (2013). Counting Fluorescent Dye Molecules on DNA Origami by Means of Photon Statistics. *Small*, *9*(23), 4061–4068. https://doi.org/10.1002/smll.201300619

Lajoie, M. J., Rovner, A. J., Goodman, D. B., Aerni, H.-R., Haimovich, A. D., Kuznetsov, G., Mercer, J. A., Wang, H. H., Carr, P. A., Mosberg, J. A., Rohland, N., Schultz, P. G., Jacobson, J. M., Rinehart, J., Church, G. M., & Isaacs, F. J. (2013). Genomically recoded organisms expand biological functions. *Science (New York, N.Y.)*, *342*(6156), 357–360. https://doi.org/10.1126/science.1241459

Lawrimore, J., Bloom, K. S., & Salmon, E. D. (2011). Point centromeres contain more than a single centromere-specific Cse4 (CENP-A) nucleosome. *The Journal of Cell Biology*, *195*(4), 573–582. https://doi.org/10.1083/jcb.201106036

Lehmann, M., Lukonin, I., Noé, F., Schmoranzer, J., Clementi, C., Loerke, D., & Haucke, V. (2019). Nanoscale coupling of endocytic pit growth and stability. *Science Advances*, *5*(11), eaax5775. https://doi.org/10.1126/sciadv.aax5775

Lin, C., Jungmann, R., Leifer, A. M., Li, C., Levner, D., Church, G. M., Shih, W. M., & Yin, P. (2012). Submicrometre geometrically encoded fluorescent barcodes self-assembled from DNA. *Nature Chemistry*, *4*(10), 832–839. https://doi.org/10.1038/nchem.1451

Lin, C., Perrault, S. D., Kwak, M., Graf, F., & Shih, W. M. (2013). Purification of DNA-origami nanostructures by rate-zonal centrifugation. *Nucleic Acids Research*, *41*(2), e40–e40. https://doi.org/10.1093/nar/gks1070

Linko, V., & Dietz, H. (2013). The enabled state of DNA nanotechnology. *Current Opinion in Biotechnology*, *24*(4), 555–561. https://doi.org/10.1016/j.copbio.2013.02.001

Liss, V., Barlag, B., Nietschke, M., & Hensel, M. (2015). Self-labelling enzymes as universal tags for fluorescence microscopy, super-resolution microscopy and electron microscopy. *Scientific Reports*, *5*(1), 17740. https://doi.org/10.1038/srep17740

Liu, N., Dai, M., Saka, S. K., & Yin, P. (2019). Super-resolution labelling with Action-PAINT. *Nature Chemistry*, 1–11. https://doi.org/10.1038/s41557-019-0325-7

Llopis, J., McCaffery, J. M., Miyawaki, A., Farquhar, M. G., & Tsien, R. Y. (1998). Measurement of cytosolic, mitochondrial, and Golgi pH in single living cells with green fluorescent proteins. *Proceedings of the National Academy of Sciences of the United States of America*, *95*(12), 6803–6808. https://doi.org/10.1073/pnas.95.12.6803

Lukinavičius, G., Umezawa, K., Olivier, N., Honigmann, A., Yang, G., Plass, T., Mueller, V., Reymond, L., Jr, I. R. C., Luo, Z.-G., Schultz, C., Lemke, E. A., Heppenstall, P., Eggeling, C., Manley, S., & Johnsson, K. (2013). A near-infrared fluorophore for live-cell super-resolution microscopy of cellular proteins. *Nature Chemistry*, *5*(2), 132–139. https://doi.org/10.1038/nchem.1546

Ma, R.-I., Kallenbach, N. R., Sheardy, R. D., Petrillo, M. L., & Seeman, N. C. (1986). Three-arm nucleic acid junctions are flexible. *Nucleic Acids Research*, *14*(24), 9745–9753. https://doi.org/10.1093/nar/14.24.9745

Mahon, M. J. (2011). pHluorin2: an enhanced, ratiometric, pH-sensitive green florescent protein. *Advances in Bioscience and Biotechnology (Print)*, *2*(3), 132–137. https://doi.org/10.4236/abb.2011.23021

Mangiameli, S. M., Merrikh, C. N., Wiggins, P. A., Elife, H. M., & 2017. (n.d.). Transcription leads to pervasive replisome instability in bacteria. *Elifesciences.Org*. https://doi.org/10.7554/elife.19848.001

Mathieu, F., Liao, S., Kopatsch, J., Wang, T., Mao, C., & Seeman, N. C. (2005). Six-helix bundles designed from DNA. *Nano Letters*, *5*(4), 661–665. https://doi.org/10.1021/nl050084f

McCormick, C. D., Akamatsu, M. S., Ti, S.-C., & Pollard, T. D. (2013). Measuring Affinities of Fission Yeast Spindle Pole Body Proteins in Live Cells across the Cell Cycle. *Biophysical Journal*, *105*(6), 1324–1335. https://doi.org/10.1016/j.bpj.2013.08.017

Miesenböck, G., Angelis, D. A. D., & Rothman, J. E. (1998). Visualizing secretion and synaptic transmission with pH-sensitive green fluorescent proteins. *Nature*, *394*(6689), 192–195. https://doi.org/10.1038/28190

Milles, S., Tyagi, S., Banterle, N., Koehler, C., VanDelinder, V., Plass, T., Neal, A. P., & Lemke, E. A. (2012). Click Strategies for Single-Molecule Protein Fluorescence. *Journal of the American Chemical Society*, *134*(11), 5187–5195. https://doi.org/10.1021/ja210587q

Newman, J. R. S., Ghaemmaghami, S., Ihmels, J., Breslow, D. K., Noble, M., DeRisi, J. L., & Weissman, J. S. (2006). Single-cell proteomic analysis of S. cerevisiae reveals the architecture of biological noise. *Nature*, *441*(7095), 840–846. https://doi.org/10.1038/nature04785

Otter, W. K. den, Renes, M. R., & Briels, W. J. (2010). Asymmetry as the Key to Clathrin Cage Assembly. *Biophysical Journal*, *99*(4), 1231–1238. https://doi.org/10.1016/j.bpj.2010.06.011

Papkovsky, D. (2009). *Live Cell Imaging*. Humana Press.

Patterson, G. H., Knobel, S. M., Sharif, W. D., Kain, S. R., & Piston, D. W. (1997). Use of the green fluorescent protein and its mutants in quantitative fluorescence microscopy. *Biophysical Journal*, *73*(5), 2782–2790. https://doi.org/10.1016/s0006-3495(97)78307-3

Pinheiro, A. V., Han, D., Shih, W. M., & Yan, H. (2011). Challenges and opportunities for structural DNA nanotechnology. *Nature Publishing Group*, *6*(12), 763–772. https://doi.org/10.1038/nnano.2011.187

Prasher, D. C., Eckenrode, V. K., Ward, W. W., Prendergast, F. G., & Cormier, M. J. (1992). Primary structure of the Aequorea victoria green-fluorescent protein. *Gene*, *111*(2), 229–233. https://doi.org/10.1016/0378-1119(92)90691-h

Presolski, S. I., Hong, V. P., & Finn, M. G. (2011). Copper-Catalyzed Azide-Alkyne Click Chemistry for Bioconjugation. *Current Protocols in Chemical Biology*, *3*(4), 153–162. https://doi.org/10.1002/9780470559277.ch110148

Renz, M. (2013). Fluorescence microscopy—A historical and technical perspective. *Cytometry Part A*, *83*(9), 767–779. https://doi.org/10.1002/cyto.a.22295

Ries, J., & Schwille, P. (2012). Fluorescence correlation spectroscopy. *Bioessays*, *34*(5), 361–368. https://doi.org/10.1002/bies.201100111

Rosen, C. B., Kodal, A. L. B., Nielsen, J. S., Schaffert, D. H., Scavenius, C., Okholm, A. H., Voigt, N. V., Enghild, J. J., Kjems, J., Tørring, T., & Gothelf, K. V. (2014). Template-directed covalent conjugation of DNA to native antibodies, transferrin and

other metal-binding proteins. *Nature Chemistry*, *6*(9), 804–809. https://doi.org/10.1038/nchem.2003

Rothemund, P. W. K. (2006). Folding DNA to create nanoscale shapes and patterns. *Nature*, *440*(7082), 297–302. https://doi.org/10.1038/nature04586

Saffarian, S., Cocucci, E., & Kirchhausen, T. (2009). Distinct Dynamics of Endocytic Clathrin-Coated Pits and Coated Plaques. *PLOS Biology*, *7*(9), e1000191-18. https://doi.org/10.1371/journal.pbio.1000191

Schlichthaerle, T., Strauss, M. T., Schueder, F., Woehrstein, J. B., & Jungmann, R. (2016). DNA nanotechnology and fluorescence applications. *Current Opinion in Biotechnology*, *39*, 41–47. https://doi.org/10.1016/j.copbio.2015.12.014

Schmied, J. J., Forthmann, C., Pibiri, E., Lalkens, B., Nickels, P., Liedl, T., & Tinnefeld, P. (2013). DNA Origami Nanopillars as Standards for Three-Dimensional Superresolution Microscopy. *Nano Letters*, *13*(2), 781–785. https://doi.org/10.1021/nl304492y

Schmied, J. J., Gietl, A., Holzmeister, P., Forthmann, C., Steinhauer, C., Dammeyer, T., & Tinnefeld, P. (2012). Fluorescence and super-resolution standards based on DNA origami. *Nature Methods*, *9*(12), 1133–1134. https://doi.org/10.1038/nmeth.2254

Schmied, J. J., Raab, M., Forthmann, C., Pibiri, E., Wünsch, B., Dammeyer, T., & Tinnefeld, P. (2014). DNA origami–based standards for quantitative fluorescence microscopy. *Nature Protocols*, *9*(6), 1367–1391. https://doi.org/10.1038/nprot.2014.079

Schwille, P. (2001). Fluorescence correlation spectroscopy and its potential for intracellular applications. *Cell Biochemistry and Biophysics*, *34*(3), 383–408. https://doi.org/10.1385/cbb:34:3:383

Seeman, N. C. (1982). Nucleic acid junctions and lattices. *Journal of Theoretical Biology*, *99*(2), 237–247. https://doi.org/10.1016/0022-5193(82)90002-9

Shaw, A., Benson, E., & Högberg, B. (2015). Purification of Functionalized DNA Origami Nanostructures. *ACS Nano*, *9*(5), 4968–4975. https://doi.org/10.1021/nn507035g

Shih, W. M., Quispe, J. D., & Joyce, G. F. (2004). A 1.7-kilobase single-stranded DNA that folds into a nanoscale octahedron. *Nature*, *427*(6975), 618–621. https://doi.org/10.1038/nature02307

Singh, J. K. D., Luu, M. T., Abbas, A., & Wickham, S. F. J. (2018). Switchable DNA-origami nanostructures that respond to their environment and their applications. *Biophysical Reviews*, *10*(5), 1283–1293. https://doi.org/10.1007/s12551-018-0462-z

Slaughter, B D, & Li, R. (2010). Toward Quantitative “In Vivo Biochemistry” with Fluorescence Fluctuation Spectroscopy. *Molecular Biology of the Cell*, *21*(24), 4306–4311. https://doi.org/10.1091/mbc.e10-05-0451

Slaughter, Brian D, Huff, J. M., Wiegraebe, W., Schwartz, J. W., & Li, R. (2008). SAM Domain-Based Protein Oligomerization Observed by Live-Cell Fluorescence Fluctuation Spectroscopy. *PloS One*, *3*(4), e1931-8. https://doi.org/10.1371/journal.pone.0001931

Sochacki, K. A., & Taraska, J. W. (2019). From Flat to Curved Clathrin: Controlling a Plastic Ratchet. *Trends in Cell Biology*, *29*(3), 241–256. https://doi.org/10.1016/j.tcb.2018.12.002

Soundrarajan, N., Sokalingam, S., Raghunathan, G., Budisa, N., Paik, H.-J., Yoo, T. H., & Lee, S.-G. (2012). Conjugation of Proteins by Installing BIO-Orthogonally Reactive Groups at Their N-Termini. *PLoS ONE*, *7*(10), e46741. https://doi.org/10.1371/journal.pone.0046741

Stahl, E., Martin, T. G., Praetorius, F., & Dietz, H. (2014). Facile and scalable preparation of pure and dense DNA origami solutions. *Angewandte Chemie International Edition*, *53*(47), 12735–12740. https://doi.org/10.1002/anie.201405991

Stein, I. H., Schüller, V., Böhm, P., Tinnefeld, P., & Liedl, T. (2011). Single-Molecule FRET Ruler Based on Rigid DNA Origami Blocks. *ChemPhysChem*, *12*(3), 689–695. https://doi.org/10.1002/cphc.201000781

Stein, J., Stehr, F., Schueler, P., Blumhardt, P., Schueder, F., Mücksch, J., Jungmann, R., & Schwille, P. (2019). Towards absolute molecular numbers in DNA-PAINT. *Nano Letters*, acs.nanolett.9b03546-30. https://doi.org/10.1021/acs.nanolett.9b03546

Straight, A. F. (2007). *Fluorescent Protein Applications in Microscopy* (Vol. 81, pp. 93–113). Elsevier. https://doi.org/10.1016/s0091-679x(06)81006-x

Takakura, H., Zhang, Y., Erdmann, R. S., Thompson, A. D., Lin, Y., McNellis, B., Rivera-Molina, F., Uno, S., Kamiya, M., Urano, Y., Rothman, J. E., Bewersdorf, J.,

Schepartz, A., & Toomre, D. (2017). Long time-lapse nanoscopy with spontaneously blinking membrane probes. *Nature Biotechnology*, 1–13. https://doi.org/10.1038/nbt.3876

The MathWorks MATLAB (9.8.0.1359463 (R2020a) Update 1). (2020). [MacOS]. The MathWorks, Inc.

Thompson, A. D., Omar, M. H., Rivera-Molina, F., Xi, Z., Koleske, A. J., Toomre, D. K., & Schepartz, A. (2017). Long-Term Live-Cell STED Nanoscopy of Primary and Cultured Cells with the Plasma Membrane HIDE Probe DiI-SiR. *Angewandte Chemie International Edition*, *56*(35), 10408–10412. https://doi.org/10.1002/anie.201704783

Thubagere, A. J., Li, W., Johnson, R. F., Chen, Z., Doroudi, S., Lee, Y. L., Izatt, G., Wittman, S., Srinivas, N., Woods, D., Winfree, E., & Qian, L. (2017). A cargo-sorting DNA robot. *Science*, *357*(6356), eaan6558. https://doi.org/10.1126/science.aan6558

Tian, Y., Martinez, M. M., & Pappas, D. (2011). Fluorescence correlation spectroscopy: a review of biochemical and microfluidic applications. *Historia: Zeitschrift Fur Alte Geschichte*, *65*(4), 115A-124A. https://doi.org/10.1366/10-06224

Tinevez, J.-Y., Perry, N., Schindelin, J., Hoopes, G. M., Reynolds, G. D., Laplantine, E., Bednarek, S. Y., Shorte, S. L., & Eliceiri, K. W. (2017). TrackMate: An open and extensible platform for single-particle tracking. *Methods (San Diego, Calif.)*, *115*, 80–90. https://doi.org/10.1016/j.ymeth.2016.09.016

Trads, J. B., Tørring, T., & Gothelf, K. V. (2017). Site-Selective Conjugation of Native Proteins with DNA. *Accounts of Chemical Research*, *50*(6), 1367–1374. https://doi.org/10.1021/acs.accounts.6b00618

Tsien, R. Y. (1998). The green fluorescent protein. *Annual Review of Biochemistry*, *67*(1), 509–544. https://doi.org/10.1146/annurev.biochem.67.1.509

Verdaasdonk, J. S., Lawrimore, J., & Bloom, K. (2014). *Determining absolute protein numbers by quantitative fluorescence microscopy* (Vol. 123, pp. 347–365). Elsevier. https://doi.org/10.1016/b978-0-12-420138-5.00019-7

Vukojević, V., Pramanik, A., Yakovleva, T., Rigler, R., Terenius, L., & Bakalkin, G. (2005). Study of molecular events in cells by fluorescence correlation spectroscopy. *Cellular and Molecular Life Sciences*, *62*(5), 535–550. https://doi.org/10.1007/s00018-004-4305-7

Wagenbauer, K. F., Engelhardt, F. A. S., Stahl, E., Hechtl, V. K., Stömmer, P., Seebacher, F., Meregalli, L., Ketterer, P., Gerling, T., & Dietz, H. (2017). How We Make DNA Origami. *ChemBioChem*, *18*(19), 1873–1885. https://doi.org/10.1002/cbic.201700377

Wang, T., Liang, C., Xu, H., An, Y., Xiao, S., Zheng, M., Liu, L., & Nie, L. (2020). Incorporation of nonstandard amino acids into proteins: principles and applications. *World Journal of Microbiology and Biotechnology*, *36*(4), 60. https://doi.org/10.1007/s11274-020-02837-y

Wassie, A. T., Zhao, Y., & Boyden, E. S. (2019). Expansion microscopy: principles and uses in biological research. *Nature Methods*, *16*(1), 33–41. https://doi.org/10.1038/s41592-018-0219-4

Werner, E. W., Mei, T.-S., Burckle, A. J., & Sigman, M. S. (2012). Enantioselective Heck arylations of acyclic alkenyl alcohols using a redox-relay strategy. *Science (New York, N.Y.)*, *338*(6113), 1455–1458. https://doi.org/10.1126/science.1229208

Wieland, G., Orthaus, S., Ohndorf, S., Diekmann, S., & Hemmerich, P. (2004). Functional Complementation of Human Centromere Protein A (CENP-A) by Cse4p from Saccharomyces cerevisiae. *Molecular and Cellular Biology*, *24*(15), 6620–6630. https://doi.org/10.1128/mcb.24.15.6620-6630.2004

Williams, N. D., Landajuela, A., Kasula, R. K., Zhou, W., Powell, J. T., Xi, Z., Isaacs, F. J., Berro, J., Toomre, D., Karatekin, E., & Lin, C. (2020). DNA-Origami-Based Fluorescence Brightness Standards for Convenient and Fast Protein Counting in Live Cells. *Nano Letters*. https://doi.org/10.1021/acs.nanolett.0c03925

Winfree, E., Liu, F., Wenzler, L. A., & Seeman, N. C. (1998). Design and self-assembly of two-dimensional DNA crystals. *Nature*, *394*(6693), 539–544. https://doi.org/10.1038/28998

Woehrstein, J. B., Strauss, M. T., Ong, L. L., Wei, B., Zhang, D. Y., Jungmann, R., & Yin, P. (2017). Sub-100-nm metafluorophores with digitally tunable optical properties self-assembled from DNA. *Science Advances*, *3*(6). https://doi.org/10.1126/sciadv.1602128

Wu, J.-Q., & Pollard, T. D. (2005). Counting cytokinesis proteins globally and locally in fission yeast. *Science (New York, N.Y.)*, *310*(5746), 310–314. https://doi.org/10.1126/science.1113230

Xia, T., Li, N., & Fang, X. (2013). Single-Molecule Fluorescence Imaging in Living Cells. *Annual Review of Physical Chemistry*, *64*(1), 459–480. https://doi.org/10.1146/annurev-physchem-040412-110127

Yang, Y. R., Liu, Y., & Yan, H. (2015). DNA Nanostructures as Programmable Biomolecular Scaffolds. *Bioconjugate Chemistry*, *26*(8), 1381–1395. https://doi.org/10.1021/acs.bioconjchem.5b00194

Zanacchi, F. C., Manzo, C., Alvarez, A. S., Derr, N. D., Garcia-Parajo, M. F., & Lakadamyali, M. (2017). A DNA origami platform for quantifying protein copy number in super-resolution. *Nature Methods*, *14*(8), 789–792. https://doi.org/10.1038/nmeth.4342

Zipfel, W. R., & Webb, W. W. (2001). *In vivo Diffusion Measurements Using Multiphoton Excitation Fluorescence Photobleaching Recovery and Fluorescence Correlation Spectroscopy* (pp. 216–235). Springer New York. https://doi.org/10.1007/978-1-4614-7513-2_13